Late Quaternary deglaciation of Prince William Sound, Alaska

Peter J. Haeussler, Ari Matmon, Maurice Arnold, Georges Aumaitre, Didier Bourles, Karim Keddadouche

Quaternary Research (2022), **105**, 115–134
doi:10.1017/qua.2021.33

Research Article

Late Quaternary deglaciation of Prince William Sound, Alaska

Peter J. Haeussler[a]*, Ari Matmon[b], Maurice Arnold[c], Georges Aumaître[c], Didier Bourlès[c] and Karim Keddadouche[c]

[a]U.S. Geological Survey, Anchorage, Alaska 99508-4626, USA; [b]Institute of Earth Sciences, Hebrew University of Jerusalem, Jerusalem 91904, Israel and [c]CEREGE, UMR 6635 CNRS-Aix-Marseille University, BP 80, 13 545 Aix-en-Provence Cedex 4, France

Abstract

To understand the timing of deglaciation of the northernmost marine-terminating glaciers of the Cordilleran Ice Sheet (CIS), we obtained 26 ^{10}Be surface-exposure ages from glacially scoured bedrock surfaces in Prince William Sound (PWS), Alaska. We sampled six elevation transects between sea level and 620 m and spanning a distance of 14 to 70 km along ice flow paths. Most transect age–elevation patterns could not be explained by a simple model of thinning ice; the patterns provide evidence for lingering ice cover and possible inheritance. A reliable set of 20 ages ranges between 17.4 ± 2.0 and 11.6 ± 2.8 ka and indicates ice receded from northwestern PWS around 14.3 ± 1.6 ka, thinned at a rate of ~120–160 m/ka, and retreated from sea-level sites at 12.9 ± 1.1 ka at a rate of 20 m/yr. The retreat rate likely slowed as glaciers retreated into northern PWS. These results are consistent with the growing body of reported deglacial constraints on collapse of ice sheets along the Alaska margin indicating collapse of the CIS soon after 17 ka. These data are consistent with paleotemperature data indicating that a warming North Pacific Ocean caused catastrophic collapse of this part of the CIS.

Keywords: Deglaciation, Prince William Sound, Alaska, ^{10}Be exposure ages, Retreat rate, Thinning rate, Cordilleran Ice Sheet

(Received 21 April 2020; accepted 3 May 2021)

INTRODUCTION

Records of deglaciation are critical to understanding the response of ice sheets to a warming climate and changing sea level, and they are essential for constraining models of changing climate (e.g., Clark et al., 2009; Vieli and Nick, 2011; Seguinot et al., 2014, 2016). They are also needed for speculation on the routes and timing of human migration into the Americas (e.g., Mandryk et al., 2001; Erlandson et al., 2011). The Cordilleran Ice Sheet (CIS) overlaid the western margin of the coastal mountain ranges of Washington, British Columbia, Yukon, and southern Alaska, with numerous marine-terminating glaciers along the Pacific margin (Fig. 1). Recent refinements constrain the terrestrial deglaciation history of much of the CIS (e.g., Stroeven et al., 2014; Balbas et al., 2017; Clague, 2017; Kopczynski et al., 2017; Menounos et al., 2017; Darvill et al., 2018; Lesnek et al., 2020), but are lacking along the southern and southwestern Alaska margin.

We examine the deglaciation of Prince William Sound (PWS), Alaska, which lies on the southern side of the northernmost extent of the CIS (Figs. 1 and 2). We aim to establish the history of deglaciation, compare it with other records from Alaska, and evaluate oceanographic and atmospheric linkages and drivers. Kaufman et al. (2011) showed the maximum limits of Pleistocene and late Wisconsinan glaciers in Alaska (Fig. 1). They state this is approximately equivalent to the last glacial maximum (LGM) at approximately 26 to 20 ka (Clark et al., 2009). Kaufman et al. (2011, p. 443) also noted, "Nowhere else in Alaska is the extent of Pleistocene glacier ice more poorly constrained than along the southern margin of the Cordilleran Ice Sheet." Thus, the marine limits of these glaciers are estimated almost everywhere on the map (Fig. 1), and in general are inferred to have extended to the edge of the continental shelf, particularly where cross-shelf troughs exist. Minor modifications to these ice limits were inferred by Haeussler et al. (2015) for a region offshore PWS and by Zimmerman et al. (2019) for a region offshore the Alaska Peninsula.

There are some recent constraints on the retreat history of marine-terminating ice for the region east of PWS. At a site on the upper continental slope (Fig. 1, location D), south of Kayak Island, Davies et al. (2011) interpreted a transition from coarse glacial-marine sediments to finely laminated sediments at 14,790 ± 380 cal yr BP as the time that tidewater glaciers to the north retreated onto land or behind fjord sills. Further southeast, west of Cross Sound (Fig. 1, location CS) and Glacier Bay, Praetorius and Mix (2014) infer significant landward retreat of glaciers between ~13 and 12.5 ka based on radiocarbon dating and changes in sediment type. Praetorius et al. (2020) also provide a paleo–sea surface temperature record for the North Pacific showing lower temperatures around 17 ka and warming until about 14.6 ka, which was followed by a cooling trend through the Younger Dryas, then followed by warming about 12.1 ka. These marine studies lead us to evaluate the deglaciation history in a region with less dramatic coastal topography and the relationships between the sea-surface temperature history on glacial thinning and retreat in PWS.

*Corresponding author: Email address: pheuslr@usgs.gov

Cite this article: Haeussler PJ, Matmon A, Arnold M, Aumaître G, Bourlès D, Keddadouche K (2022). Late Quaternary deglaciation of Prince William Sound, Alaska. *Quaternary Research* **105**, 115–134. https://doi.org/10.1017/qua.2021.33

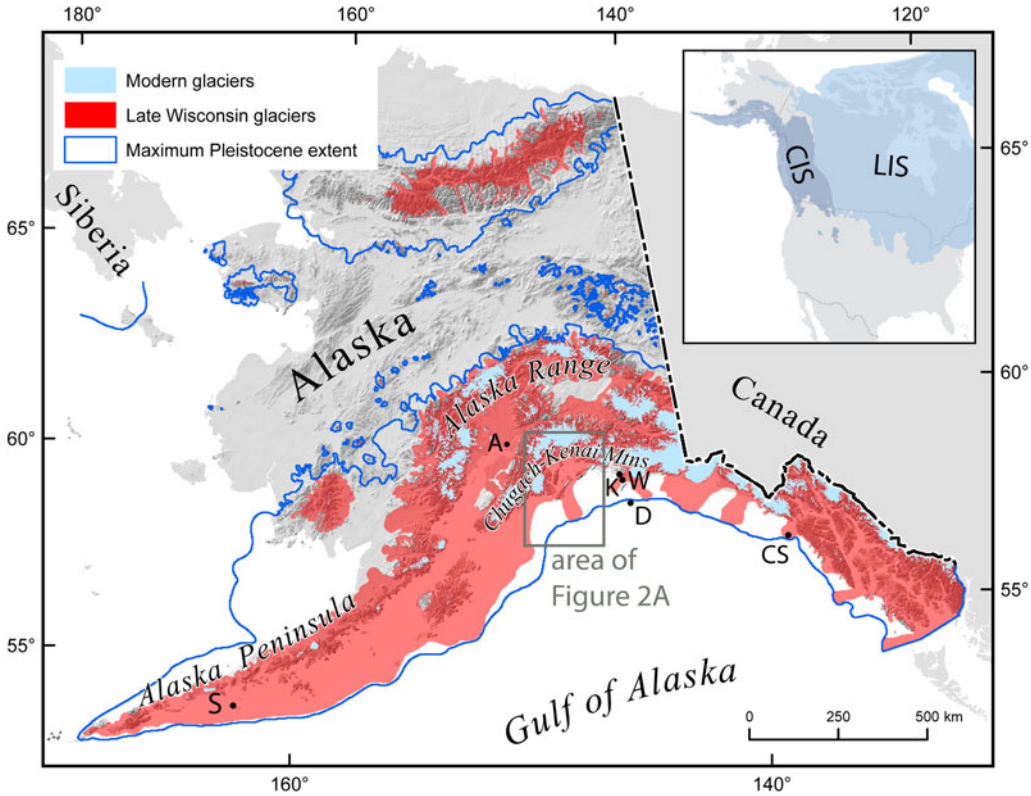

Figure 1. Late Wisconsinan (approximately last glacial maximum) and Pleistocene maximum extent of glaciers in Alaska, modified from Kaufman et al. (2011). Inset map shows the position of these glaciers with respect to the Cordilleran Ice Sheet (CIS) and the Laurentide Ice Sheet (LIS) in North America (glacial extents from Batchelor et al., 2019). Note the asymmetry of late Wisconsinan glaciers on the southern Alaska margin, with glaciers covering almost the entire landscape in contrast to the north side of the Alaska Range and Alaska Peninsula, which had short glaciers, due to rain shadow effects. Modern glaciers, in light blue, show the location of high topography. Inset box shows location of study area in Fig. 2A. Black dots with letter labels: A, Anchorage; K, Katalla; S, Sanak Island; W, Wingham Island. Location D refers to core EW0408 85JC discussed in Davies et al. (2011), and location CS refers to core EW0408 66JC offshore Cross Sound discussed in Praetorius and Mix (2014).

Only two radiocarbon ages from within PWS constrain the timing of glacial retreat soon after the LGM. One of these ages is from a sample collected near the town of Valdez (Fig. 2, location V), where a basal peat overlying till gave a ^{14}C age of 14,020 ± 770 cal yr BP (Reger, 1990; Table 1). This unique exposure was found during large excavations related to construction of an oil-transportation facility. Heusser (1983) found and analyzed another basal peat in Port Wells (Fig. 2, location G), which has an age of 11,580 ± 220 cal yr BP (Table 1). Both localities are in northern PWS, far north of the shelf edge, and thus deglaciation of more distal regions likely began earlier than roughly 14,000 yr BP. More recent Neoglacial and Little Ice Age (LIA) and retreats of glaciers in the last 4 ka are well studied in PWS and adjacent areas (e.g., Wiles et al., 1999; Barclay et al., 2009), but not the late Quaternary deglaciation. As we could not date moraines, our approach to examining deglacial timing was through cosmogenic radionuclide (CRN) exposure dating of vertical profiles of glacially striated surfaces on islands that serve as "dipsticks" for the thickness of glaciers that were within PWS. This dipstick approach has been successfully used in a number of locations to quantify glacial thinning (e.g., Stone et al., 2003; Mackintosh et al., 2007; Corbett et al., 2019).

GEOLOGIC AND GEOGRAPHIC SETTING

The rocks in PWS are part of a vast accretionary complex of Paleocene–Eocene age (e.g., Plafker et al., 1994). These dominantly metasedimentary rocks were intruded by granitic plutons during Paleocene to Eocene time; some mafic volcanic rocks are also present (Nelson et al., 1985; Bradley et al., 2003). The rocks were subsequently exhumed in middle to late Cenozoic time (Arkle et al., 2013; Ferguson et al., 2015), forming the present mountainous landscape. The region lies above the shallowly dipping Alaska–Aleutian subduction zone, which last ruptured in 1964 in a M_w9.2 earthquake (Plafker, 1969), which is the second largest earthquake ever recorded. Paleoseismological studies indicate earthquakes of similar magnitude occur on average every ~535 yr (Shennan et al., 2014), causing strong ground shaking, landslides, and toppling of rocks and boulders. Today, and in the past (Kaufman et al., 2011), there has been a strong asymmetry to the length of glaciers on either side of the Chugach and Kenai Mountains that flank PWS (see Fig. 1), because storm systems travel northeasterly from the Aleutians and have prevailing southerly winds (Shulski and Wendler, 2007). Glaciers filled almost the entire landscape on the southern sides of the coastal mountains, in contrast to the northern sides, which had relatively short glaciers.

The physiography of the region is of a three-sided bowl, with high mountains on the north, east, and west sides, where glaciers still cover most of the landscape above ~700 m (Figs. 1 and 2). The highest peaks of the Chugach Mountains, with summits as high as 4016 m, lie at the northwestern edge of PWS. The central part of PWS has islands with rounded summits indicating glacial sculpting, presumably during the LGM. The bathymetry includes a series of troughs and shows that trunk glaciers

https://doi.org/10.1017/qua.2021.33 Published online by Cambridge University Press

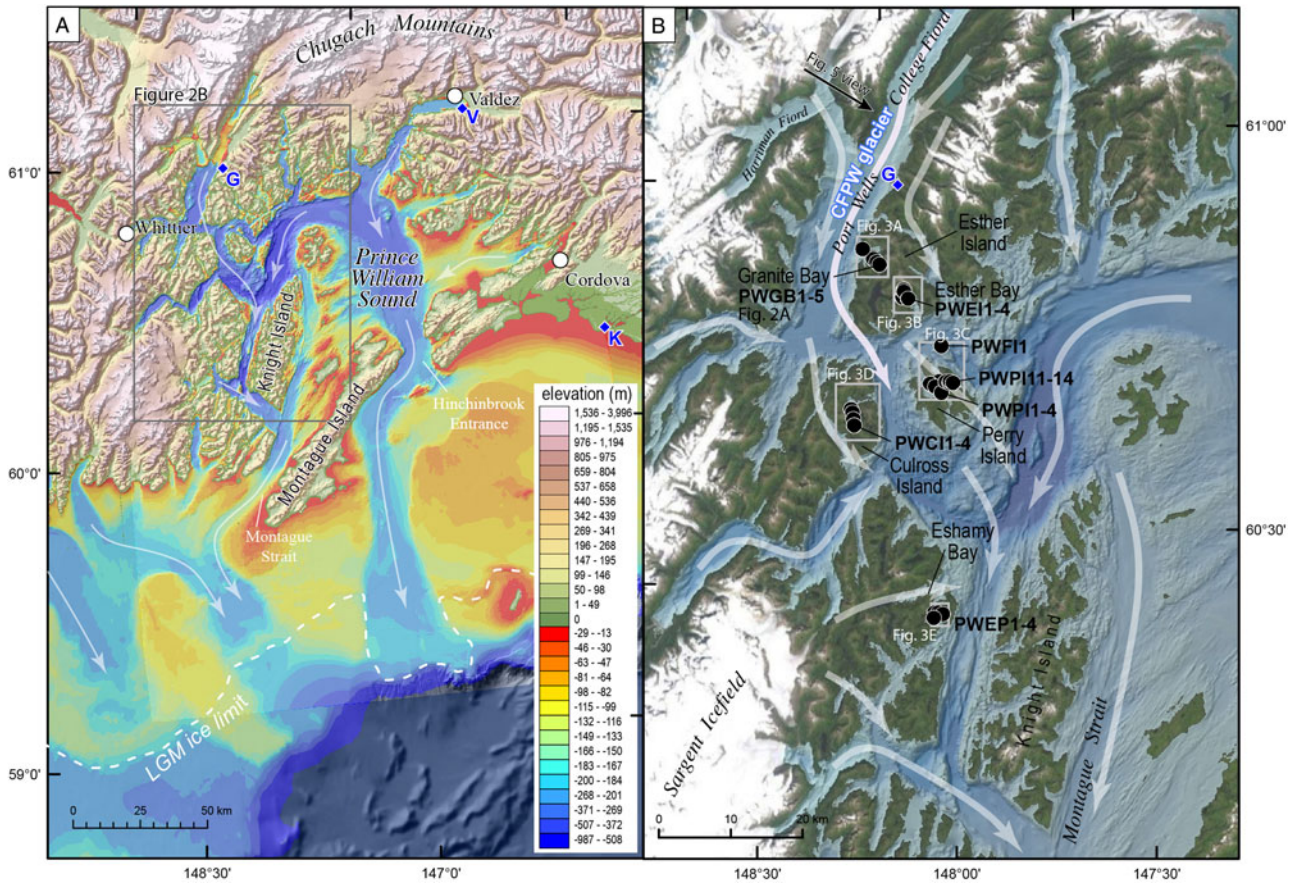

Figure 2. Geographic setting of the Prince William Sound (PWS) and cosmogenic radionuclide (CRN) sampling sites. (A) Overview of topography and bathymetry of PWS. White arrows show the flow direction of major glaciers and ice streams at last glacial maximum (LGM) time from Kaufman et al. (2011) with minor modifications from Haeussler et al. (2015). Blue diamonds labeled G, V, and K are locations of prior ^{14}C dates (see text and Table 1). G, Golden; V, Valdez; K, Katalla. Location of Fig. 2B is shown and labeled. (B) A more detailed view of northwestern PWS showing sampling areas and locations of site maps shown in Fig. 3. White arrows show inferred LGM glacial flow directions from aligned valleys and glacial striae. CFPW glacier is the College Fiord–Port Wells glacier that is inferred to have covered all of the sampling sites, except those sites in the area of Fig. 3E, which was covered by a glacier emanating from the Sargent Icefield.

Table 1. Basal radiocarbon ages in and near Prince William Sound, Alaska.

Location	Sample number	Elevation (m)	Material dated	Radiocarbon age (yr BP)	Error (yr)	Calibrated age: mean (yr BP)	1 sigma (yr)	Calibrated age[a]: median (yr BP)	95.4% probability (yr BP)	Data source
Valdez	a[b]	113	Twigs, moss, and organic silt	11,820	560	14,020	770	13,920	15,610–12,700	Reger (1990)
Golden	G-1 250 cm	4	Organic silt	10,015	125	11,580	220	11,560	12,000–11,220	Heusser (1983)
Wingham Island	WingRC18	20	Peat	12,040	60	13,890	90	13,890	14,060–13,750	Chapman et al. (2009)
Tiekel Bog	I-3,796	494	Silty peat	13,900	400	16,850	550	16,850	17,930–15,790	Sirkin and Tuthill (1987)

[a]All samples calibrated using OxCal v. 4.3.2 (Bronk Ramsey, 2017) and IntCal13 (Reimer et al., 2013).
[b]Laboratory number GX-10789.

exited PWS through Hinchinbrook Entrance and Montague Straight (Fig. 2). Kaufman and Manley (2004) and Kaufman et al. (2011) inferred that glaciers extended to the edge of the continental shelf at LGM time. The terrestrial Quaternary geology of PWS has never been studied in detail, and only bedrock geologic maps exist of the region (e.g., Nelson et al., 1985). Late Quaternary and Holocene deposits consist of alluvial sand and gravel in valley bottoms, small LIA moraines, and colluvial deposits (e.g., Nelson et al., 1985; Wiles et al., 1999). Bedrock bedding, faults, and fractures are clearly visible where not obscured by vegetation, showing the entire landscape was abraded by glaciers during glacial maxima. Finally, given glacial retreat, we assume there was glacial-isostatic

https://doi.org/10.1017/qua.2021.33 Published online by Cambridge University Press

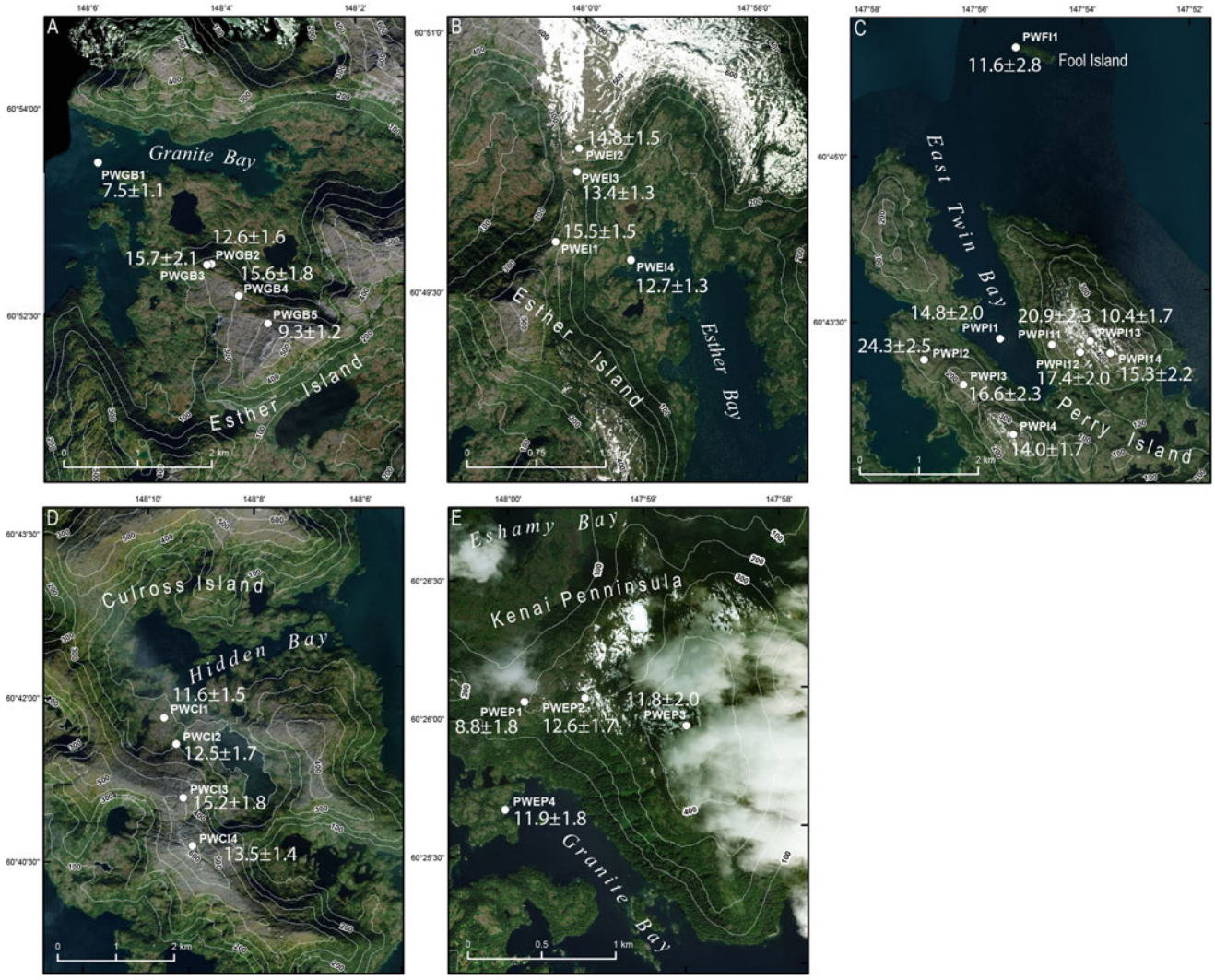

Figure 3

Figure 3. Maps of sampling sites and cosmogenic ages, in kiloyears (Table 3, column with GIA correction). See Fig. 2B for locations within Prince William Sound. Background satellite image from Esri World Imagery compilation (https://services.arcgisonline.com/ArcGIS/rest/services/World_Imagery/MapServer/0, accessed 28 May 2021). (A) Sampling area near Granite Bay on Esther Island. We refer to this area as "Granite Bay" or "Granite Bay on Esther Island." (B) Sampling area near Esther Bay on Esther Island. We refer to this area as "Esther Bay." (C) We sampled the ridges on the east and west sides of East Twin Bay on Perry Island. We refer to these transects as "Perry-East" or "Perry-West." In our summary plots, both transects share a sampling site (PWPI1) in the middle of the bay. Note the solitary Fool Island sample site lies to the north. (D) Sampling area near Hidden Bay on Culross Island. We refer to this sampling area as "Culross." (E) This sampling area lies near Eshamy Bay, and we refer to this sampling transect as "Eshamy."

adjustment (GIA). However, evidence for this uplift in the form of terraces or uplifted marine deposits has not been reported in the literature (see the compilation of Shugar et al., 2014), and we have not seen such features.

SAMPLING STRATEGY, SITES, AND METHODS

To better understand the timing of glacial thinning and retreat in PWS, we sampled quartz-bearing granitic bedrock to date the exposure of glacially scoured surfaces using cosmogenic ^{10}Be (Fig. 3). Using the typical cosmogenic exposure method to date boulders in moraines (e.g., Ivy-Ochs and Briner, 2014) was not possible, because the terminal moraines are offshore and underwater, and no other LGM moraines are mapped to examine. For sampling scoured bedrock, we looked for locations with varying distances along paleo–ice streams and for locations where we could collect a suite of samples in a small area that would provide a vertical transect that might allow us to document the thinning of an ice sheet. We chose locations as far as practical from modern valley and alpine glaciers, so they would be unaffected by Neoglacial ice advances (Barclay et al., 2009), such as in the Harriman Fiord area (Fig. 2B). We also looked for locations with rounded summits, because this morphology implies that glaciers overran the surface. During our fieldwork, we examined numerous outcrops of both the metasedimentary and granitic rocks. Although we could find undulatory and scoured surfaces on metasedimentary rocks indicative of glacial scour, we were unable to find any clear glacial striae. The rocks were often highly weathered and fractured, indicating surface lowering since exposure, and poor in quartz, making them mediocre candidates for cosmogenic exposure dating. We exclusively sampled granitic rock, because it contains abundant quartz, and we targeted

https://doi.org/10.1017/qua.2021.33 Published online by Cambridge University Press

Figure 4. Glacial features at sampling sites. All photographs by PJH, U.S. Geological Survey. (A) Smooth scoured and striated surface above Esther Bay, on Esther Island at site PWEI1, which is located at a pass (see Fig. 3B). Person is holding their arms parallel to the striae. (B) At sea-level elevation, sample site PWPI1 in East Twin Bay on Perry Island (see Fig. 3C). Person is standing on rockweed (*Fucus distichus*), which grows up to approximately mean high tide level. Left of the person's leg is a mafic boulder; the closest outcrop of this rock type occurs 25 km to the southeast. We infer the boulder must have been ice rafted to the present location. (C) At the rounded summit of Perry Island at site PWPI4 (Fig. 3C), showing glacial polish and striae, which point toward ice overtopping this island and coming from the direction of Port Wells. (D) Glacial striae and grooves near the summit of Culross Island near site PWCI4. (E) Glacial grooves and plucked faces from Fool Island (Fig. 3C). (F) Typical expression of 1–3 mm of positive relief of a mafic enclave. This shows that surface lowering of the granites is inconsequential for the cosmogenic ages.

bedrock outcrops hosting well-preserved glacial scour features, grooves, polish, pluck marks, and striae (Fig. 4). Although bedrock outcrops can be susceptible to ^{10}Be inheritance (e.g., Brook et al., 1993; Ivy-Ochs and Briner, 2014), we did not sample any boulders because (1) we found no exposed moraines; (2) erratics perched on bedrock often appeared toppled by frost jacking or earthquake shaking; and (3) erratics on mountaintops and ridges were either nonexistent or rare. We sampled five main sites on three islands and a mainland peninsula (Figs. 2 and 3). Most samples came from broad ridges that lacked soils, had little vegetation, and minimized topographic shielding. This study was limited by the lack of paired boulder and bedrock samples, and we were unable to directly test for cosmogenic inheritance.

Tidewater glaciers remain in northern and western PWS, and at LGM time these glaciers would have overrun the sampling localities (Fig. 2). Glacial striations, grooves, roche moutonnée, and drainage patterns indicate that a large trunk glacier, which we refer to as the "CFPW Glacier," flowed down College Fiord and Port Wells and overran Esther, Culross, and Perry Islands (Fig. 2B). This glacier, which may have been an ice stream, flowed toward central PWS and ultimately exited the sound through Montague Strait (Fig. 2). We observed stranded hanging glacial troughs north of Esther Island, parallel to College Fiord and Port Wells (Fig. 5). These U-shaped troughs are oriented north-northwesterly and indicate the margins of the CFPW glacier once blanketed the mountains on the east side of the fjord. It is reasonable to assume this same large CFPW glacier overran Esther Island, producing its rounded summits. Farther south, the CFPW glacier overran Culross and Perry Islands with their rounded summits. Glacial striae on the summits of Perry and Culross Islands point toward Port Wells and are consistent with this inferred ice flow direction (Fig. 4C and D). The one sampling locality that did not have the CFPW glacier as its source is near Eshamy Bay. This locality had ice sourced from the nearby Sargent Ice Field that lies 20 km to the west (see Figs. 2B and 3D). Eshamy Bay is a U-shaped, east-west trending valley, with a broad U-shaped saddle at its western end. This geomorphology demonstrates eastward ice flow from the Sargent Ice Field down the bay and over the sampling locality. Given the proximity of this site to the modern Sargent Icefield, this site was closer to the paleo–ice source than any of the others.

https://doi.org/10.1017/qua.2021.33 Published online by Cambridge University Press

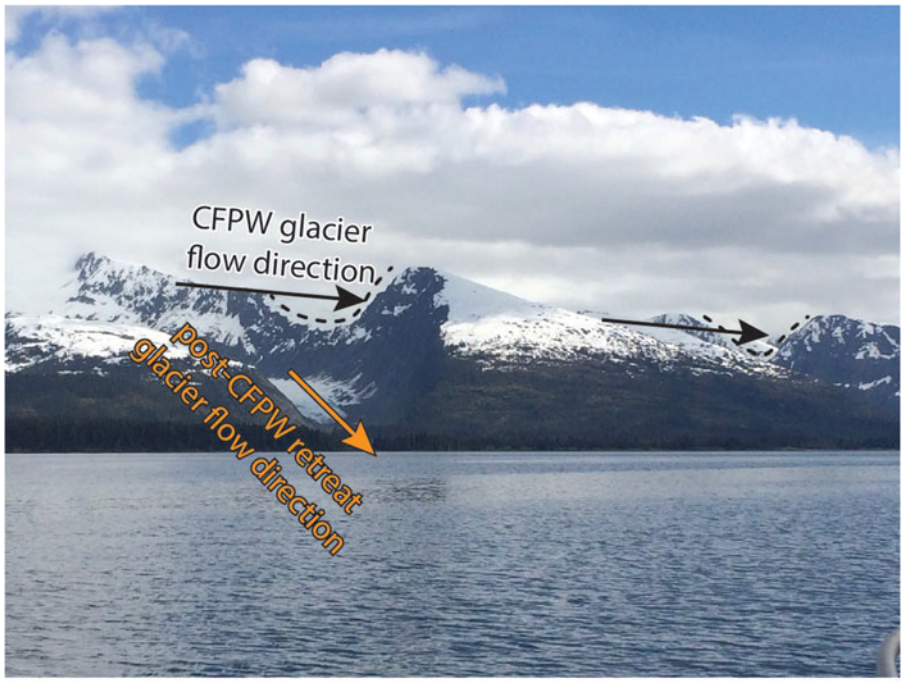

Figure 5. Abandoned hanging glacial valleys, outlined by dashed lines, to the north-northwest of Esther Island near Coghill Lake (location on Fig. 2B). The black lines and arrows show the south-southeastward flow direction of a former College Fiord–Port Wells (CFPW) glacier. After the CFPW glacier retreated, the valleys were abandoned and then cut by glaciers flowing westward (orange arrow) at a right angle to the previously thicker and wider CFPW glacier. Photograph by PJH, U.S. Geological Survey.

We found essentially no evidence of postglacial erosion of granitic rock surfaces as shown by the features on Figure 4. Surfaces with glacial polish have had no weathering (Fig. 4C). On some surfaces with glacial scour, but lacking polish, we observed mafic enclaves that had a positive relief of 1–3 mm (Fig. 4F). Thus, the mafic enclaves are more resistant to weathering than the granite and indicate minimal postexposure surface lowering, which is insignificant for calculating cosmogenic exposure ages. Moreover, none of our sites had any evidence of prior cover such as till or soil that subsequently was eroded.

In total, we collected 26 bedrock samples from four islands and a site on the Kenai Peninsula in the western PWS (Figs. 2 and 3, Table 2). These include:

1. Five samples from Granite Bay on the northwest side of Esther Island (Fig. 3A, PWBG samples). These five samples were along an elevation transect that ranges between 0 and 420 m above sea level (m asl). For convenience, we refer to this as the "Granite Bay" transect. We collected four more samples on the southeast side of the island along an elevation transect that ranges between 5 and 349 m asl (Fig. 3B, PWEI samples) near Esther Bay. We refer to this as the "Esther Bay" transect.
2. Eight samples from Perry Island (Fig. 3C, PWPI samples). These were collected along two elevation transects (four samples from each transect). The eastern transect ranges in elevation between 0 and 360 m asl, which we refer to as "Perry-East." The western transect ranges in elevation between 178 and 503 m, which we refer to as "Perry-West." Both transects share sampling site PWPI1 in the middle of the bay.
3. One sample from Fool Island (Fig. 3C, PWFI samples), which is located about 2.5 km north-northeast of Perry Island at an elevation of 3 m asl.
4. Four samples from Culross Island (Fig. 3D, PWCI samples) along an elevation transect between 131 and 620 m asl, which we refer to as the "Culross" transect.
5. Four samples from near Eshamy Bay (Fig. 3E, PWEP samples) along a transect that ranges between 4 and 498 m asl. We refer to this as the "Eshamy" transect.

Samples were collected using a hammer and chisels, and the maximum thickness of all samples collected was 3.0 cm. Samples were prepared at the Cosmogenic Laboratory of the Hebrew University of Jerusalem following procedures slightly modified from Corbett et al. (2016) and Kohl and Nishiizumi (1992). Our field estimates of quartz content determined the size of the collected samples. However, during sample preparation, we found the quartz content was lower than estimated in the field, leading to a low yield. Quartz yield for each sample ranges from 4.74 to 13.38 g (Table 2). This low yield added to the relatively high uncertainty (10%–24% with an average of 13 ± 3%) of the calculated ages. $^{10}Be/^{9}Be$ ratios were measured by the accelerator mass spectrometry facility (ASTER) at CEREGE, Aix-en-Provence, France (Table 2).

For calculation of ^{10}Be exposure ages, we used the iceTEA online interface (Jones et al., 2019a; ice-tea.org, accessed 28 May 2021), which uses a modified version of the CRONUScalc calculation framework of Marrero et al. (2016) and global production rate calibration data sets of Borchers et al. (2016). Within iceTEA, we used the "LSD" scaling scheme (Lifton et al., 2014), which applies a sea-level, high-latitude ^{10}Be production rate of 4.09 atoms/g SiO_2/yr and a ^{10}Be decay constant of 4.99×10^{-7}/yr. We opted to use the iceTEA calculator, rather than the more common calculator, formerly known as CRONUS-Earth, because it is the only one that can also do GIA calculations. The GIA calculator includes corrections for a changing time–altitude history, such as

https://doi.org/10.1017/qua.2021.33 Published online by Cambridge University Press

Table 2. Geographic and analyical data for Prince William Sound samples.

Samplea	Location	Latitude (°N)	Longitude (°W)	Distance from ice source (km)	Elevation (m above sea level)	Thickness (cm)[a]	Production rate (atoms/g/yr)		Shielding factor[b]	Dendation rate (mm/yr)	Quartz (g)[c]	Added weight of Be (mg)[d]	$^{10}Be/^{9}Be$[e,f]	^{10}Be (atoms/g SiO_2)[f,g,h]
							Spallation	Muons						
PWEI1	Esther Bay, Esther Island	60.82895	148.01020	55	321	3	5.74	0.17	0.998079	0	11.579	0.259	6.311E-14±2.389E-15	94,341.87±4039.70
PWEI2	Esther Bay, Esther Island	60.83777	148.00385	55	349	3	5.85	0.17	0.988451	0	11.936	0.260	6.286E-14±3.455E-15	91,652.70±5360.01
PWEI3	Esther Bay, Esther Island	60.83553	148.00470	55	262	3	5.41	0.17	0.997554	0	11.877	0.276	4.987E-14±2.533E-15	77,397.52±4225.04
PWEI4	Esther Bay, Esther Island	60.82653	147.99553	55	5	3	4.15	0.14	0.986666	0	10.569	0.255	3.535E-14±1.963E-15	56,955.47±3361.49
PWPI11	West Twin Bay, Perry Island	60.71890	147.91878	68	178	3	4.98	0.16	0.992948	0	12.227	0.265	7.543E-14±4.861E-15	109,091.60±7361.19
PWPI12	West Twin Bay, Perry Island	60.71733	147.91018	68	266	3	5.45	0.17	0.979797	0	13.378	0.262	7.503E-14±5.077E-15	98,125.02±6923.91
PWPI13	West Twin Bay, Perry Island	60.71895	147.90683	68	400	3	6.17	0.18	0.997042	0	6.844	0.263	2.651E-14±3.747E-15	68,128.81±9725.90
PWPI14	West Twin Bay, Perry Island	60.71680	147.90093	68	503	3	6.78	0.19	1.000000	0	12.45	0.253	8.063E-14±9.149E-15	10,9673.34±12637.35
PWPI1	East Twin Bay, Perry Island	60.72052	147.93460	67	0	3	4.10	0.14	0.996950	0	7.162	0.221	3.243E-14±3.317E-15	66,750.39±6955.99
PWPI2	East Twin Bay, Perry Island	60.71838	147.95877	67	181	3	4.95	0.16	0.999761	0	7.056	0.228	5.927E-14±2.947E-15	12,7806.73±6848.99
PWPI3	East Twin Bay, Perry Island	60.71413	147.94727	67	233	3	5.26	0.16	0.999953	0	7.572	0.267	3.936E-14±3.910E-15	92,839.87±9408.78
PWPI4	East Twin Bay, Perry Island	60.70593	147.93325	67	360	3	5.92	0.18	0.999999	0	7.858	0.262	3.968E-14±3.629E-15	88,285.06±8264.70
PWFI1	Fool Island	60.76418	147.92145	64	3	3	4.14	0.14	0.999888	0	8.111	0.255	2.490E-14±5.862E-15	52,218.92±12336.80
PWGB1	Granite Bay, Esther Island	60.89297	148.10070	47	0	3	4.10	0.14	0.997895	0	8.641	0.252	1.717E-14±2.553E-15	33,422.81±5013.87
PWGB2	Granite Bay, Esther Island	60.87952	148.07470	47	243	3	5.31	0.16	0.998150	0	7.571	0.238	3.387E-14±3.122E-15	71,020.61±6699.56
PWGB3	Granite Bay, Esther Island	60.87948	148.07578	47	231	3	5.30	0.16	0.997944	0	7.091	0.276	3.370E-14±3.208E-15	87,580.01±8519.21
PWGB4	Granite Bay, Esther Island	60.87540	148.06862	47	317	3	5.72	0.17	0.999288	0	7.085	0.257	3.888E-14±2.803E-15	94,376.49±7061.36
PWGB5	Granite Bay, Esther Island	60.87175	148.06195	47	420	3	6.30	0.18	0.996133	0	7.441	0.269	2.547E-14±2.562E-15	61,451.71±6302.64

(*Continued*)

https://doi.org/10.1017/qua.2021.33 Published online by Cambridge University Press

Table 2. (*Continued.*)

Samplea	Location	Latitude (°N)	Longitude (°W)	Distance from ice source (km)	Elevation (m above sea level)	Thickness (cm)[a]	Production rate (atoms/g/yr)		Shielding factor[b]	Dendation rate (mm/yr)	Quartz (g)[c]	Added weight of Be (mg)[d]	$^{10}Be/^{9}Be$[e,f]	^{10}Be (atoms/g SiO_2)[f,g,h]
							Spallation	Muons						
PWCI1	Hidden Bay, Culross Island	60.69542	148.16745	70	131	3	4.74	0.15	0.995330	0	8.785	0.242	3.189E-14±3.164E-15	58,661.79±5937.81
PWCI2	Hidden Bay, Culross Island	60.69123	148.16438	70	192	3	5.05	0.16	0.994234	0	8.768	0.239	3.686E-14±3.824E-15	67,133.62±7093.87
PWCI3	Hidden Bay, Culross Island	60.68292	148.16365	70	493	3	6.73	0.19	0.998123	0	8.733	0.257	5.485E-14±4.103E-15	10,8031.77±8365.20
PWCI4	Hidden Bay, Culross Island	60.67548	148.16212	70	620	3	7.54	0.20	1.000000	0	7.975	0.303	4.260E-14±2.552E-15	10,8023.27±6822.54
PWEP1	Eshamy Bay, mainland	60.43398	148.00013	14	196	3	5.07	0.16	0.998980	0	7.669	0.271	2.010E-14±3.519E-15	47,548.09±8378.99
PWEP2	Eshamy Bay, mainland	60.43388	147.99262	14	283	3	5.52	0.17	0.999239	0	7.633	0.256	3.299E-14±3.656E-15	73,928.94±8325.67
PWEP3	Eshamy Bay, mainland	60.43167	147.98047	14	498	3	6.76	0.19	0.999945	0	4.74	0.277	2.160E-14±3.086E-15	84,402.41±12176.22
PWEP4	Eshamy Bay, mainland	60.42758	148.00370	14	4	3	4.14	0.14	0.994213	0	8.147	0.327	2.003E-14±2.771E-15	53,669.45±7501.81

[a]The tops of all samples were exposed at the surface.
[b]Calculated using CRONUS-Earth online calculator v. 2, revised April 2018.
[c]A density of 2.7 g/cm^3 was used based on the granitic compostion of the surface samples.
[d]10Be/9Be ratio of added Be ranges between 3.26×10^{-15} and 8.07×10^{-15}.
[e]Isotope ratios were normalized to ^{10}Be CEREGE in house standard with a mean value of 5.60×10^{-12} and using a ^{10}Be half-life of 1.387×10^{6} yr.
[f]Uncertainties reported at the 1σ confidence level.
[g]Reported values are corrected for respective procedural blanks in each batch. Blank values range between 3.26×10^{-15} and 8.07×10^{-15}.
[h]Propagated uncertainties include error in the blank and counting statistics.

Table 3. Exposure ages of Prince William Sound samples.

		LSD scaling model			With 15 cm annual snow cover			With 50 cm annual snow cover			With 100 cm annual snow cover			With GIA correction[a]			
Sample	Elevation (m)	^{10}Be age (yr)	Measurement uncertainty (1σ; yr)	Total uncertainty (1σ; yr)	^{10}Be age (yr)	Measurement uncertainty (1σ; yr)	Total uncertainty (1σ; yr)	^{10}Be age (yr)	Measurement uncertainty (1σ; yr)	Total uncertainty (1σ; yr)	^{10}Be age (yr)	Measurement uncertainty (1σ; yr)	Total uncertainty (1σ; yr)	^{10}Be age (yr)	Total uncertainty (1σ; yr)	Mean age difference (yr)	% difference of uncorrected age
PWEI1	321	15,600	670	1490	16,020	690	1490	17,050	720	1620	18,630	800	1720	15,540	1510	−60	−0.38
PWEI2	349	14,910	860	1540	15,310	890	1570	16,290	970	1690	17,810	1010	1850	14,840	1530	−70	−0.47
PWEI3	262	13,510	750	1360	13,880	760	1370	14,770	810	1490	16,140	910	1630	13,440	1340	−70	−0.52
PWEI4	5	12,800	720	1340	13,150	760	1360	13,990	810	1410	15,290	900	1570	12,730	1290	−70	−0.55
PWPI11	178	20,700	1390	2230	21,260	1420	2270	22,630	1560	2430	24,740	1690	2650	20,860	2320	160	0.77
PWPI12	266	17,390	1240	1920	17,860	1240	1960	19,010	1330	2120	20,770	1480	2280	17,380	1970	0	0.00
PWPI13	400	10,460	1500	1740	10,750	1610	1870	11,460	1590	1910	12,510	1800	2070	10,420	1740	−40	−0.38
PWPI14	503	15,320	1780	2180	15,730	1850	2270	16,740	1960	2420	18,300	2060	2590	15,260	2200	−60	−0.39
PWPI1	0	14,910	1560	2000	15,310	1610	2050	16,300	1640	2150	17,810	1940	2420	14,840	2020	−70	−0.47
PWPI2	181	24,010	1310	2370	24,670	1330	2460	26,260	1410	2590	28,710	1580	2880	24,330	2480	320	1.33
PWPI3	233	16,610	1710	2190	17,060	1740	2220	18,160	1870	2400	19,850	2020	2620	16,580	2270	−30	−0.18
PWPI4	360	14,050	1360	1810	14,430	1360	1790	15,360	1440	1920	16,780	1560	2130	13,980	1730	−80	−0.57
PWFI1	3	11,610	2680	2830	11,920	2890	3050	12,690	2910	3100	13,860	3390	3580	11,550	2820	−50	−0.43
PWGB1[b]	0	7460	1050	1170	7650	1050	1210	8130	1190	1360	8900	1260	1500	7450	1130	−10	−0.13
PWGB2	243	12,610	1230	1580	12,950	1250	1660	13,790	1260	1720	15,070	1420	1900	12,550	1580	−60	−0.48
PWGB3	231	15,740	1560	2040	16,160	1580	2070	17,210	1670	2210	18,810	1880	2470	15,700	2060	−50	−0.32
PWGB4	317	15,640	1200	1770	16,060	1200	1780	17,100	1240	1930	18,680	1380	2070	15,590	1810	−50	−0.32
PWGB5	420	9270	910	1180	9510	1000	1230	10,140	960	1270	11,100	1040	1360	9250	1220	−20	−0.22
PWCI1	131	11,600	1120	1480	11,910	1230	1540	12,680	1290	1670	13,850	1450	1870	11,550	1480	−60	−0.52
PWCI2	192	12,550	1320	1700	12,890	1300	1720	13,710	1480	1850	14,990	1560	2020	12,490	1660	−60	−0.48
PWCI3	493	15,250	1190	1740	15,660	1220	1790	16,670	1310	1900	18,210	1470	2100	15,190	1770	−60	−0.39
PWCI4	620	13,580	830	1420	13,950	900	1490	14,840	950	1540	16,210	1050	1700	13,510	1410	−70	−0.52
PWEP1	196	8780	1610	1780	9020	1630	1780	9600	1760	1930	10,510	1830	2020	8760	1820	−30	−0.34
PWEP2	283	12,620	1470	1780	12,970	1500	1850	13,800	1490	1910	15,080	1690	2110	12550	1730	−70	−0.55
PWEP3	498	11,840	1720	2000	12,160	1720	2000	12,940	1880	2160	14,130	2030	2330	11,780	1990	−70	−0.59
PWEP4	4	11,970	1690	1950	12,290	1680	1980	13,080	1870	2150	14,300	1950	2280	11,910	1840	−60	−0.50
averages:	268	14,133	1335	1817	14,515	1374	1865	15,451	1447	1980	16,886	1596	2169	14,103	1824	−31	−0.30

[a]Without a snow cover correction. GIA, glacial-isostatic adjustment.
[b]Culled: see text; averages at bottom of columns do not include this sample.

during sea-level low stands and submergence of samples, before isostatic adjustment. Due to overcast skies and fog while collecting some samples, we opted for a uniform geographic information systems (GIS) approach to calculating topographic shielding at each site (Table 2). We used the r.horizon tool in the GRASS set of raster tools (grass.osgeo.org, accessed 28 May 2021) for the open-source QGIS software (qgis.org, accessed 28 May 2021) to calculate the angle from horizontal to the horizon at each site.

RESULTS

Overall, ^{10}Be concentrations range between 33,423 ± 5,014 and 127,807 ± 6849 atoms/g quartz (Table 2). Sea-level elevation samples (0–5 m asl; n = 5) yielded ^{10}Be concentrations ranging between 33,423 ± 5014 and 66,750 ± 5956 atoms/g quartz with a mean of 52,603 ± 12,127 atoms/g quartz. Apart from sample PWGB1, sea-level samples exhibit a relatively small scatter in ^{10}Be concentrations (mean = 57,399 ± 6542 atoms/g quartz), indicating similar and straightforward exposure histories. The highest-elevation samples in each transect (349–620 m asl; n = 6) yielded ^{10}Be concentrations that range between 61,451 ± 6303 and 109,673 ± 12,637 atoms/g quartz. These concentrations correlate weakly with elevation (r^2 = 0.26), indicating that the differences in concentrations are controlled by varying exposure histories rather than simply by elevation. This trend is also expressed by the observations that the highest ^{10}Be concentration was measured in a sample that was collected from an elevation of only 181 m (PWPI2) and that, overall, the highest ^{10}Be concentrations (>100,000 atoms/g quartz) were derived from samples that were collected from elevations that range between 178 and 620 m asl.

Evaluation of snow shielding and GIA on ages

^{10}Be concentrations have simple, uncorrected, ages that range between 7.5 ± 1.0 and 24.0 ± 2.4 ka (Table 3). However, ^{10}Be concentrations and, by inference, exposure ages are influenced by several processes, such as snow shielding and GIA, which are not considered in the uncorrected ages. Let us first consider the influence of snow cover. Before about 11 ka, global temperatures were colder than today (Seguinot et al., 2016; Praetorius et al., 2020), and we infer more snow cover at our sampling sites. Present climate is remarkably varied within the PWS region, with mean annual snowfall varying from 313 to 502 cm at weather stations within 100 km of our sampling localities (Blanchet, 1983). There are few quantitative data for snow cover, in contrast to precipitation. Only one location within the study area has snow cover data: Esther Island, elevation 15 m (Natural Resources Conservation Service automated SNOTEL site (https://www.wcc.nrcs.usda.gov/snow/, accessed 28 May 2021)), has almost complete data from the interval of 2013 to 2020 and some data from three previous years. The data show snow cover from November to May, which yielded average values of November, 4.6 cm; December, 10.8 cm; January, 17.3 cm; February, 49.5 cm; March, 56.8 cm; April, 59.0; and May, 0.6 cm; a year-round average of 16.5 cm. Snow cover is also elevation dependent, as the snowpack melts more slowly at higher elevations. None of the sites have perennial snow fields today. Finally, snow cover is dependent on wind, which can be high on ridges or mountaintops, where most of our samples were collected, and can reduce or eliminate snow cover.

To evaluate the effects of snow cover, we ran several scenarios, including 15, 50, and 100 cm of annual snow cover (Table 3). As an example, if there were 15 cm of snow cover evenly on all sites for 12 months a year (a rounded average of the SNOTEL site on Esther Island), ages would average about 400 yr or 2.7% older (see Table 3). This is probably a minimum snow cover correction, but if it annually averaged 50 or 100 cm, such as at higher altitudes, and particularly before 11 ka (Seguinot et al., 2016; Praetorius et al., 2020), the correction is exponentially greater—about 1300 yr (9.3%) and 2700 yr (19.5%), respectively (Table 3). Given the lack of a reasonable way to estimate snow cover and the additional variabilities related to elevation and aspect, we did not apply a snow-shielding correction. Thus, our exposure ages are a minimum, the true ages are likely 400+ yr older, with possibly higher values at higher elevations.

^{10}Be ages are sensitive to atmospheric depth; therefore, changes in elevation due to isostatic rebound as well as the sea-level history have the potential to affect cosmogenic radionuclide ages (Jones et al., 2019b). In particular, it is possible that samples collected close to present-day sea level were submerged, and thus shielded, for a period of time soon after deglaciation, before isostatic rebound, and then re-exposed after GIA. Chapman et al. (2009) evaluated the isostatic rebound and sea-level rise at Wingham Island, Alaska (Fig. 1)—about 110 km to the southeast of PWS—in a region that likely has a similar glacial history and crustal thickness and rigidity. They assumed the total sea-level rise in southern Alaska since 20 ka was 120–135 m, and they modeled total isostatic rebound during the past 16 ka to be about 130 m. The similarity between the magnitude of sea-level rise and isostatic rebound calculated by Chapman et al. (2009) suggests that our samples would have remained above sea level and were not shielded by seawater. However, Chapman et al. (2009) argue that sea-level rise outpaced isostatic rebound between 20 and 9 ka, based on work by Clague and James (2002), who studied the British Columbia, Canada, margin. Thus, five of our samples that are located within a few meters of sea level may have been covered and shielded by seawater for part of that time period, indicating that these samples would yield minimum ages.

To calculate the effects of GIA and possible seawater shielding during sea-level rise on the ^{10}Be ages in our study, we utilized the iceTEA set of tools (Jones et al., 2019a). For the GIA correction, we used the ICE-6G model of Peltier et al. (2015), as it is the most advanced global model available. ICE-6G uses the deglaciation isochrones for North America from a compilation by Dyke et al. (2003). That data set is significantly more robust for deglaciation of the Laurentide and Innuitian Ice Sheets than for the CIS in Alaska. However, the general pattern and timing of deglaciation in Alaska appears to be in accord with the maximum Wisconsinan glacial extents reported by Kaufman and Manley (2004) and Kaufman et al. (2011), as well as the other constraints reported in the introduction. ICE-6G also models a global sea-level curve. The model does not account for the specific rheology for the lithosphere of southern Alaska, nor does it include more recent constraints on the mantle viscosity in southeastern Alaska (Larsen et al., 2005). Moreover, there are no constraints on the magnitude or timing of the GIA in PWS (Shugar et al., 2014). We acknowledge these model limitations, as we lack a more robust method for evaluating GIA and sea-level rise. A unique feature of iceTEA calculations is that they will have a production rate of zero if the sample is submerged and falls below sea level.

The modeling of our results shows the iceTEA GIA correction has a small effect on the calculated ages, resulting in changes from −70 yr to +320 yr (Table 3). The average change is −31 yr, and the largest changes are with the oldest samples, which would have

https://doi.org/10.1017/qua.2021.33 Published online by Cambridge University Press

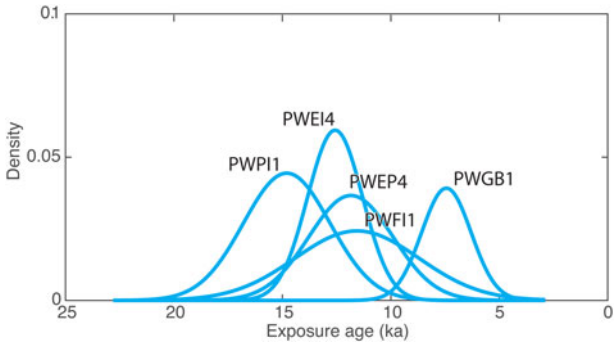

Figure 6. Kernel density distributions of ^{10}Be exposure ages of samples collected between 0 and 5 m above sea level (m asl). Ages are glacial-isostatic adjustment corrected and use the LSD scaling model (Table 3).

experienced the largest adjustment in altitude relative to sea level. All of the corrected ages are within 1.33% of the original ages. We use these elevation-corrected ages for the remainder of our discussion (Fig. 3, Table 3).

DISCUSSION AND INTERPRETATION

In spite of the uncertainties associated with our exposure ages, we proceed with our discussion assuming these calculated ages approximate the timing of bedrock exposure from deglaciation. We first discuss samples at sea level, then examine details of the variation in ages in each vertical transect, and then discuss aspects of all transects when considered together.

Sea-level samples

Exposure ages of sea-level samples can reflect a complex history, because they are most likely to be affected by GIA and sea-level rise. Five samples were collected between 0 and 5 m asl (PWEI4, PWPI1, PWFI1, PWGB1, PWEP4) and yielded exposure ages based on their present elevations that range between 7.4 ± 1.1 and 14.8 ± 2.0 ka (Fig. 3, Table 3). Given the relative proximity of the samples to one another, we would expect them to have the same GIA and sea-level history. Sample PWGB1 from Granite Bay is the youngest of our samples, and the 1σ error from this sample does not overlap the 1σ errors from any of the other samples. A kernel density estimate of the probability distribution function (Lowell, 1995) as implemented in iceTEA (Jones et al., 2019a) shows the probability distribution function of this sample has some overlap with the others (Fig. 6), but because the age of this sample is significantly younger than the others, it is an outlier and does not share the same geologic history as the other samples.

There is no geologic evidence that the timing of deglaciation at sea level between the Granite Bay site and the other nearby sites should be different. The geomorphology shows no evidence of glacial stagnation between Granite Bay and the nearby bays. Alternatively, if the young age of PWGB1 is related to a glacier remaining in its valley for a longer period of time, we would expect all of the ^{10}Be ages from this locality to be significantly younger. However, this is not the case, and the nearby Esther Bay samples have similar ages. The older postglacial radiocarbon age to the north (Table 1, Golden sample,) is also not consistent with a young sea-level age at Granite Bay. Anomalously high snow cover could shield the site and make it appear younger. However, there is no reason to hypothesize why this site, but not others nearby, would have additional snow. On reexamination of the site (Fig. 7), we determined that the smooth surface we sampled was likely caused by removal of an exfoliation slab and not by glacial scour. Parallel joint surfaces above and below the sampled surface and a few granitic boulders remain on the outcrop, consistent with debris related to breakup of an exfoliation slab. Exfoliation after glaciation is a common phenomenon (e.g., Gilbert, 1904), and we infer that the smooth surface we sampled was exposed by the removal of an exfoliation slab and not by glacial scour. This would result in a lower ^{10}Be concentration and hence a younger exposure age that does

Figure 7. Photograph of site PWGB1 that has fractures, parallel to and above and below the surface that is being sampled, which dip to the right. We interpret these as exfoliation fractures. Photograph by PJH, U.S. Geological Survey.

https://doi.org/10.1017/qua.2021.33 Published online by Cambridge University Press

not represent the time of deglaciation. Thus, we culled sample PWGB1 from our data set. Without sample PWGB1, we infer glaciers retreated from the sea-level sites by about 12.9 ± 1.1 ka.

Vertical transects and thinning

We plotted the GIA-corrected ages versus elevation to assess the thinning of glaciers at each site and to examine the variability of ages within and between sites (Fig. 8). Most ages lie between 9 and 15 ka (Table 3). If the data and sites provided simple records of glacier thinning, then we would expect older ages at the top and younger ages at lower elevations as glacial ice thinned (Fig. 9A). The Culross transect data form this pattern, except for the uppermost age, which is slightly younger than the next highest age, although the age lies within the error (Fig. 8C).

None of the remaining sites have similarly simple age–elevation patterns, so we considered possibilities for variations from the simple dipstick model (Fig. 9). If snow or ice remained on top of a mountain for a period of time after a glacier thinned around it—either from lingering snow and ice or due to seasonal snow cover—this would lead to younger surface exposure ages due to shielding (Fig. 9B). The only transect with significantly younger ages at the top is the Granite Bay transect, where the highest sample (PWGB5) age is 9.3 ± 1.2 ka compared with the next highest sample (PWGB4), which has an age of 15.6 ± 1.8 ka (Fig. 8B). The slightly younger age of the sample at the summit of Culross Island (PWCI4, 13.5 ± 1.4 ka) compared with the next highest sample (PWCI3), which has an age of 15.2 ± 1.8 ka, can also be explained by this mechanism, although the ages of the two samples are the same within error (Fig. 8C). The second-highest sample on the Perry East transect (PWPI13, 10.4 ± 1.7 ka; Fig. 8D) might also be explained by this mechanism. However, because the summit sample is about 5 ka older (15.3 ± 2.2 ka), it suggests a small glacier or ice field remained near the ridge where PWPI13 lies (Fig. 3C) but did not cover the summit.

Cirque glaciers and snow fields remain on the landscape longer than trunk glaciers, which explains some variations in exposure ages (Fig. 9C). The age of PWEP1 (8.8 ± 1.8 ka) from the Eshamy transect appears to fit this explanation (Fig. 8A). This sample was from the north side of a saddle, where a lingering glacier or snow field would be expected to remain after ice retreated from surrounding lower elevations. Also, the age of PWGB2 (12.6 ± 1.6 ka) from the Granite Bay transect is about 3 ka younger than nearby sample PWGB3 and next higher sample PWGB4. Both of those samples were taken from a broad ridge crest, but PWGB2 was taken at the head of a north-facing cirque. However, the age is not anomalous when compared with others in the data set (such as PWEI4, PWCI2, PWEP2). Both the Culross and Perry East transects also have samples from within cirques but do not fit this expected pattern.

Yet another scenario involves deglaciation of a rognon (an isolated rounded rock surrounded by a glacier), where rock is first exposed on the downstream side of an ice flow (Fig. 9D). None of our transects are on the downstream side of the ice flow directions, so we cannot test this. The two Perry Island ages from about 180 m elevation are the oldest in the entire data set (PWPI2, 24.3 ± 2.5 ka; PWPI11, 20.9 ± 2.3 ka; Fig. 8D.). However, they are on the upstream side of ice flow and at relatively low elevation, and the rognon mechanism cannot explain their unexpectedly old ages. We suspect some inheritance may explain their old ages, but without adjacent boulder sample ages, we cannot test this hypothesis. Inheritance occurs when ice does not erode ~2–3 m of a previously exposed rock surface. Ages can be inheritance skewed if less than that amount of rock is eroded. Inheritance has been noted in other studies (e.g., Brook et al., 1993; Briner and Swanson, 1998), as well as in midslope settings in other Arctic regions (Young et al., 2018). Because highly erosive wet-based glaciers are expected for the PWS region, we would expect deep erosion during the LGM glaciation. Nonetheless, these unexpectedly old ages are puzzling; they point to inheritance or inheritance-skewed ages, and this mechanism might affect other samples too.

When we compare exposure histories of the vertical transects (Fig. 8E), most profiles have a crudely Z-shaped appearance, with younger ages at the high and low elevations, and the oldest ages somewhere in the middle. Where an island has more than one profile, the transects are similar. For example, on Perry Island, the vertical transects are about 2 km apart on either side of East Twin Bay (Fig. 3C) and have ages within error of each other (Fig. 8D). These profiles have the oldest exposure ages around 180 m elevation of 20.9 ± 2.3 and 24.3 ± 2.5 ka, which we suspect are influenced by inheritance, as discussed earlier. The Esther Island transects at Esther Bay and Granite Bay are about 6 km apart on different aspects of the island and have similar patterns (Fig. 8B), with maximum exposure ages at about 320 m of 15.5 and 15.6 ka. When we compare all transect age–elevation plots together (Fig. 8E), the transects vary considerably, with ages converging toward the sea-level ages between 11.6 and 14.8 ka. The vertical transect patterns thus reveal details of the deglaciation processes.

Given these possible explanations for variability in transect ages, we evaluate the potential for a quantitative record of ice thinning in our data set. As mentioned before, the Culross transect appears to be the best-behaved set of data. If we cull additional outlier ages from the other transects, based on the foregoing discussion, the age patterns are clearer (Fig. 8F). For this plot, we cull PWPI2 and PWPI11 for suspicions of their being too old due to inheritance; PWEP1 for possibly being too young due to a lingering cirque glacier; and PWCI1, PWPI3, and PWGB5 due to snow shielding, as discussed previously. In this version of the plot, the remaining 20 samples yield ages that range between 11.6 ± 2.8 and 17.4 ± 2.0 ka.

We used a calculator within iceTEA to estimate the rate of ice thinning. We assume thinning was continuous over the time period of the analysis. IceTEA uses a weighted least-squares linear regression applied randomly to a 2σ normal distribution of exposure ages through 5000 iterations of a Monte Carlo simulation (Jones et al., 2019a). We grouped two pairs of transects to provide a more robust estimate of thinning. Because the Granite Bay and Esther Island transects are nearby and have similar values, we combined them and included the Fool Island sample as an additional sea-level age. Also, the Perry East and West transects are close to each other, and the age–elevation profiles are similar, so we combined them. We show results and statistics for the resulting four vertical transects (Fig. 10). The modal and median values, respectively, are 150 and 160 m/ka for the Culross transect (Fig. 10A), 50 and 130 m/ka for the Eshamy transect (Fig. 10B), 120 and 130 m/ka for the combined Granite Bay and Esther Bay transects (Fig. 10C), and 150 and 230 m/ka for the combined Perry East and West transects (Fig. 10D). The thinning-rate values of 120 to 150 m/ka are relatively consistent among all the transects. Although the rates encompassed by the 68% or 95% uncertainties are significantly larger, the relative consistency of the median and mode suggests they reflect the thinning process.

https://doi.org/10.1017/qua.2021.33 Published online by Cambridge University Press

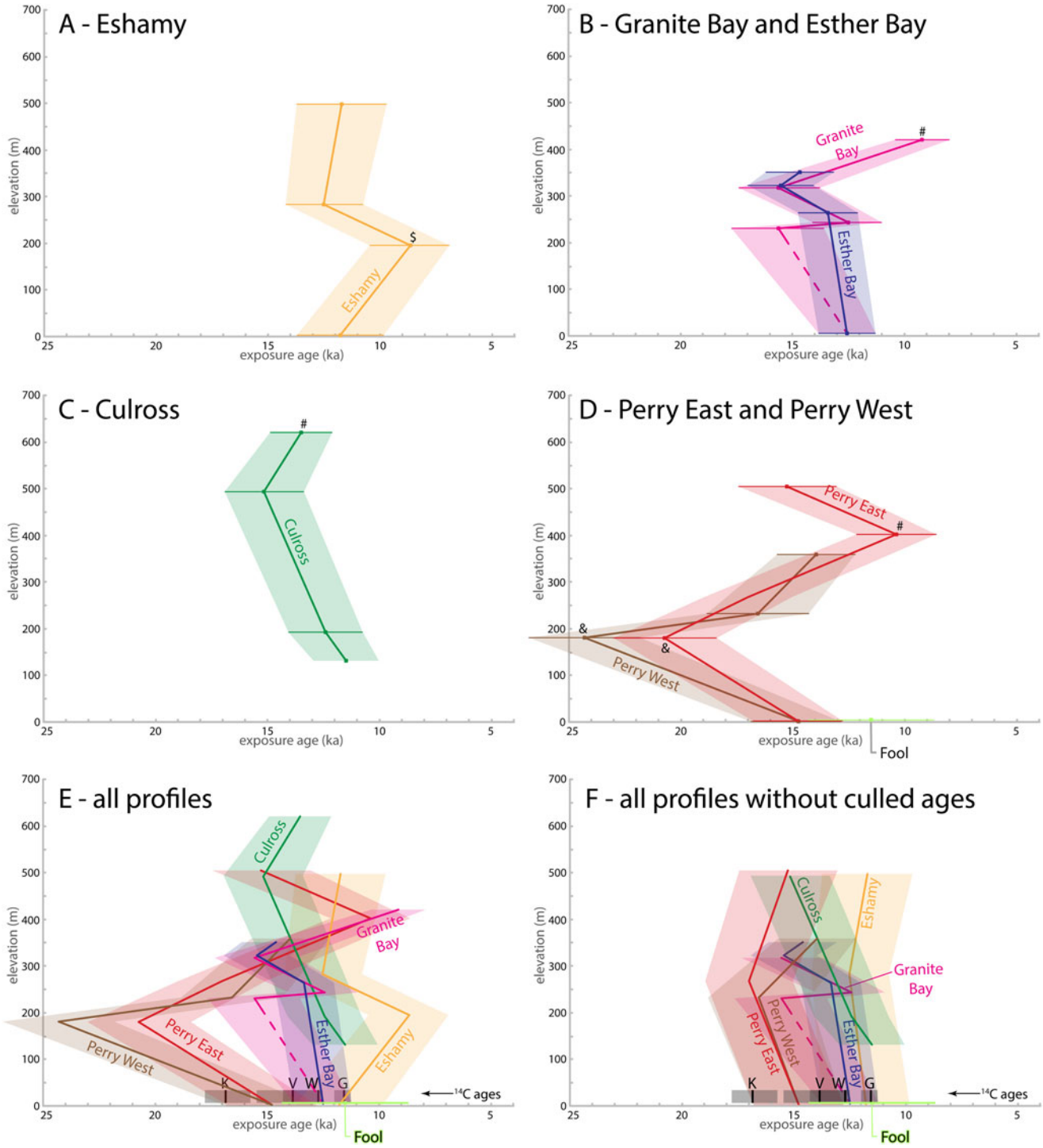

Figure 8. ^{10}Be age–elevation plots for vertical transects in the study. Dots show sample data, with horizontal thin lines showing 1σ errors; thicker lines are drawn through calculated ages; and shaded area encompasses the 1σ errors. Vertical and horizontal scales are the same for all plots. Symbols adjacent to some samples indicate suspicions of issues with ages due to #, lingering ice, snow fields, or perennial snow cover; $, lingering cirque glacier; &, possible inheritance. See text for discussion. (A) Eshamy transect (yellow). (B) Granite Bay on Esther Island (violet) and Esther Bay (blue) plots. We plot these two together, because they are located close together on different parts of the same island (Fig. 2B). For a sea-level age for Granite Bay, we plot the sea-level age from Esther Bay. (C) Culross transect (green). (D) Perry-West (brown) and Perry-East (red) transects. We plot these together, because they lie within 2 km of each other and share the sea-level sample PWPI1. We also plot the one Fool Island sample here, as it is located about 2.5 km north of Perry Island. (E) All age–elevation transects plotted together, with the same colors as in A–D. Also shown at bottom with the black lines and gray boxes for errors are postglacial ^{14}C ages discussed in the text: V, Valdez sample (Table 1); G, Golden sample (Table 1); K, Katalla sample (calibrated from Sirkin and Tuthill, 1987); W, Wingham sample (calibrated from Chapman et al., 2009). Sample locations shown on Figs. 1 or 2. (F) Plot, similar to E, except with a highly culled version of the data, in which samples PWPI2 and PWPI11 are removed for suspicion of being too old due to inheritance (denoted by & next to samples); samples PWCI1 and PWGB5 are removed for suspicion of being too young due to lingering ice, snow fields, or perennial snow cover (denoted by # next to sample); and PWEP1 (denoted by $ next to symbol) is removed for suspicion of a lingering cirque glacier.

https://doi.org/10.1017/qua.2021.33 Published online by Cambridge University Press

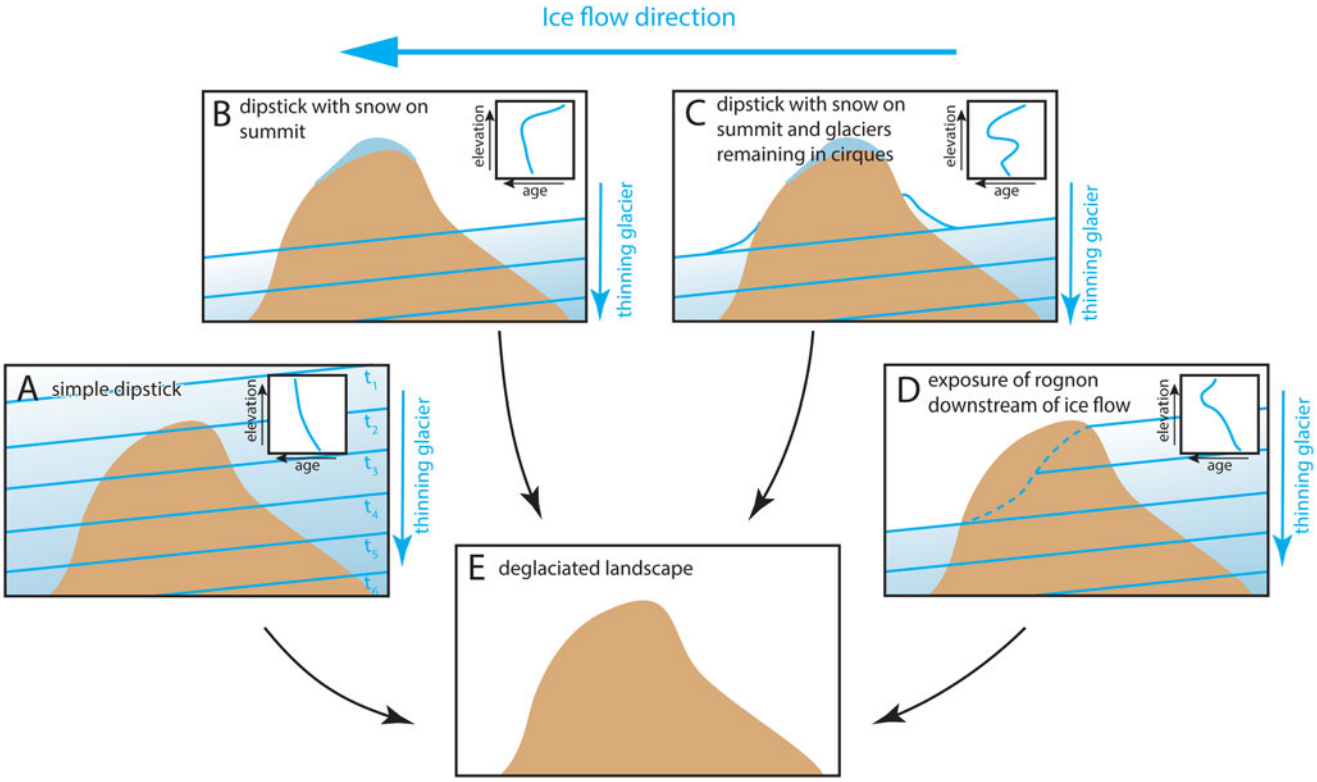

Figure 9. Cartoons showing different ways that islands can act as dipsticks in glacial flow and record thinning in surface exposure ages. View is a cross section of an island perpendicular to ice flow direction. Blue subhorizontal lines are isochrones of ice thinning at arbitrary times. Inset box shows a hypothetical age–elevation plot with the blue line showing the trend through the data. (A) Island acts as simple dipstick in ice flow, with ice thinning evenly around island. Arbitrary times t_1 (older) to t_6 (younger) are labeled here, but not in other parts of figure. (B) Simple thinning but with snow field remaining on or near summit. (C) Thinning with snow remaining on summit and with cirque glaciers feeding into the trunk glacier or alternatively remaining behind after a trunk glacier retreats. (D) Thinning of glacier exposing a rognon. (E) Final deglaciated landscape.

Moreover, these regressions have a sea-level intercept consistent with the sea-level average age of 12.9 ± 1.1 ka. These thinning rates are not as high as has been documented in the northeastern United States or in Antarctica (Johnson et al., 2014; Corbett et al., 2019), where rates are up to 590 m/ka. This difference may be due to the high topography, large catchment, and high precipitation in southern Alaska. We conclude the localities we sampled were not ideal glacial dipsticks, owing to local topography, seasonal snow cover, lingering ice, and possible cosmogenic inheritance. Nevertheless, our data reveal details of the deglaciation and erosional processes.

Ice retreat

We examined the data for evidence of glacial retreat. If we use the culled data set discussed in the previous section, the transect ages and distance to the paleo–ice source moderately correlate (Fig. 8F). The Eshamy transect is closest to the paleo–ice source and has the youngest ages. The Granite Bay and Esther Bay transects are similar and are next farthest from the paleo–ice source. The Fool Island sea-level sample is located 5 km from the mouth of Esther Bay, and its age (PWFI1, 11.6 ± 2.8 ka) is within error of the sea-level sample from nearby Esther Bay (PWEI4, 12.7 ± 1.3 ka). The similar Perry East and West transects have the oldest ages of any transect and are the farthest from a paleo–ice source. Moreover, the sea-level sample shared by both transects is the oldest of the sea-level population (PWPI1, 14.8 ± 2.0 ka). That this sample age is older than the nearby Fool Island and Esther Bay samples suggests the retreating ice front may have paused between Perry and Fool Islands. The two lowest ages on the Culross transect (PWCI1, 11.6 ± 1.5 ka; PWCI2, 12.5 ± 1.7 ka), when compared with the others, indicate that glacial ice lingered in this valley longer than in nearby Perry, Fool, and Esther Islands. The Culross Island samples are from Hidden Bay (Fig. 3D). The entrance to this bay is shallow (≤8 m), and the glacier filling this valley would not have been marine terminating at a sea-level low stand. Thus, during the thinning process, we infer a glacier remained in this valley longer than the adjacent marine-terminating trunk glacier.

A more analytical approach to examining retreat is by linear regression of the age and distance from ice source data. We applied the iceTEA calculator to the culled data set discussed earlier using the same method as for ice thinning. The calculated retreat rate is 20 m/yr (Fig. 11). The plot shows the regression is strongly influenced by the Eshamy data, which lie considerably closer to the ice source, and moreover, a different ice source than the other sites. Without the Eshamy transect, the ages of the remaining sites are considerably scattered and do not exhibit any clear age-versus-distance trend. Given the relatively small variation in distance to the ice source, perhaps this outcome is expected. If we assume all these ages (except Eshamy) are from one population, the weighted mean age is 14.3 ± 1.6 ka. These ages may not all be from one population due to factors already

https://doi.org/10.1017/qua.2021.33 Published online by Cambridge University Press

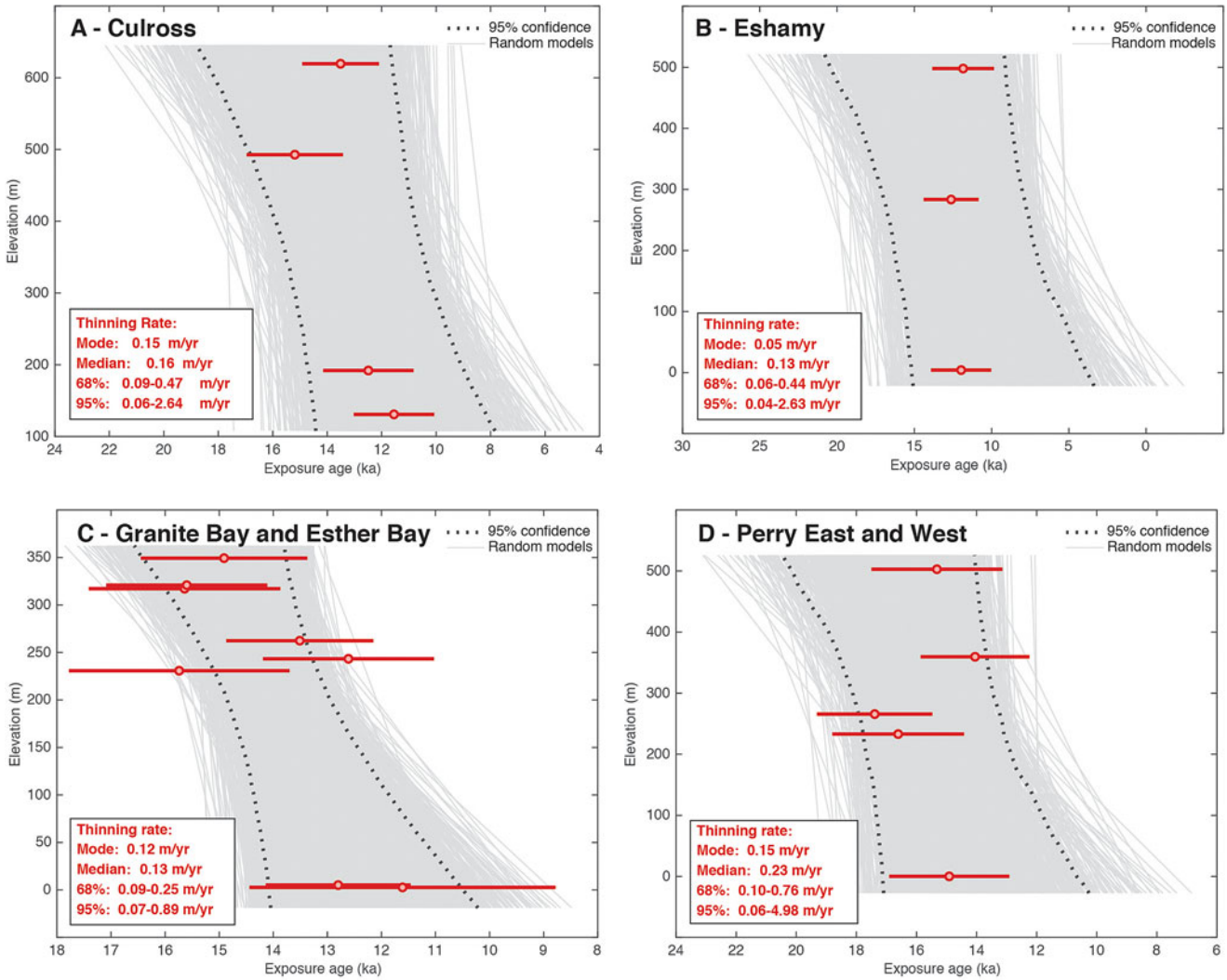

Figure 10. Plots of exposure age versus elevation for transects used for thinning-rate calculations. These plots use the highly culled data set described in the text. A weighted least-squares regression was applied randomly to normally distributed exposure ages (red dots and 1σ error bars) through 5000 iterations of Monte Carlo simulations (gray lines) with a positive slope using the iceTEA tool of Jones et al. (2019a). The statistics for these simulations are summarized in the box at the lower left of each plot, the 95% confidence limits of the thinning rate are shown with dotted black lines. (A) Culross transect, (B) Eshamy transect, (C) combined Granite Bay and Esther Bay transects, (D) combined Perry-East and Perry-West transects.

described (different elevations, snow shielding, and inheritance), but given the relative consistency of the ages and the consistent rates of thinning, we infer this is the time these mountainous islands were first exposed in this part of PWS. If we assume the Eshamy ages are from a separate population, the weighted mean of those ages is 12.2 ± 0.4 ka, indicating the Eshamy surface exposure ages are younger than the remainder of our data set. The previously discussed weighted mean of the sea-level ages is 12.9 ± 1.1 ka, which we infer is the retreat of marine-terminating glaciers past the sampling sites. The Eshamy transect ages are within the error of the sea-level ages, which indicates rapid collapse of that part of the Sargent Ice Field ice sheet.

The retreat rate may have changed as deglaciation progressed. We assume that glaciers extended locally to the edge of the continental shelf 23 ka in cross-shelf troughs (Kaufman et al., 2011; Figs. 1 and 2). The distance from Culross Island or Perry Island to the edge of the shelf is about 200 km. If we use the age of 14.3 ± 1.6 ka for removal of ice near Perry, Culross, and Esther Islands, then ice would have retreated 200 km between 23 and 14.3 ka, or during an interval of 8.7 ka. This yields a retreat rate of 23 m/yr, which is about the same rate (20 m/yr) that we calculated between our sites closer to the source of the ice. If retreat from the shelf edge was later, at ~17 ka, as suggested by Misarti et al. (2012) and Lesnek et al. (2020), then the initial retreat rate would have been 74 m/yr, which then slowed to 20 m/yr as glaciers receded toward the higher mountains that could generate more ice.

REGIONAL COMPARISONS AND GLOBAL LINKAGES

Our PWS surface exposure ages help to clarify ice retreat patterns of the northernmost marine-terminating glaciers of the CIS (Fig. 12). The two postglacial radiocarbon ages in PWS are consistent with our surface exposure ages. The older of the two basal peat ages (14,020 ± 770 cal yr BP; Reger, 1990; Fig. 12, Table 1) is nearly the same as the weighted mean of our ^{10}Be ages (14.3 ± 1.6 ka,

https://doi.org/10.1017/qua.2021.33 Published online by Cambridge University Press

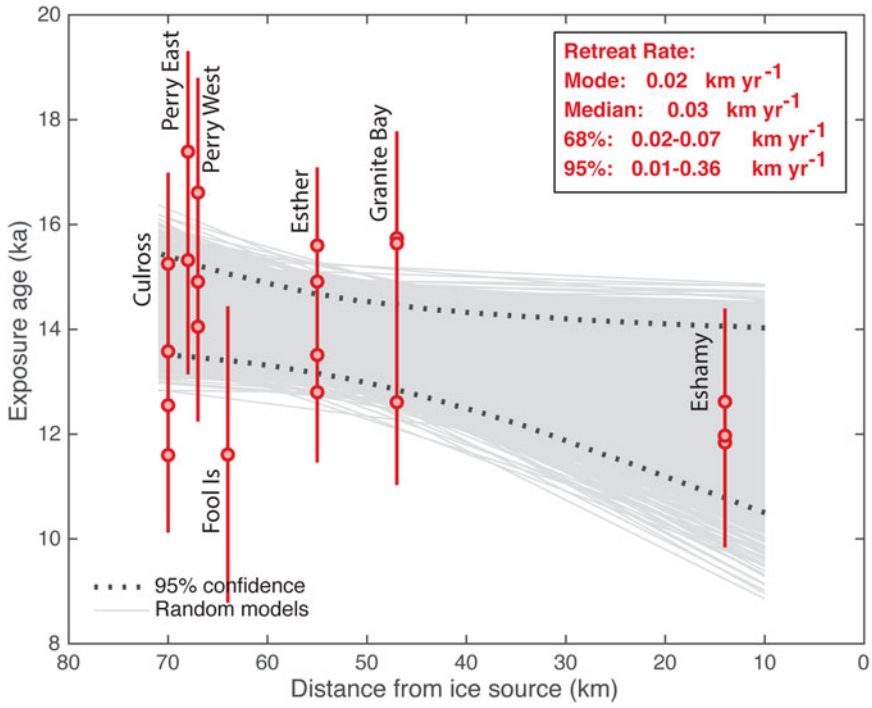

Figure 11. Exposure ages vs. distance from ice source. Transect names are labeled. The weighted least-squares regression is applied randomly to normally distributed exposure ages (red dots and 1σ error bars) through 5000 iterations of Monte Carlo simulations (gray lines) with a positive slope using the iceTEA tool of Jones et al. (2019a).

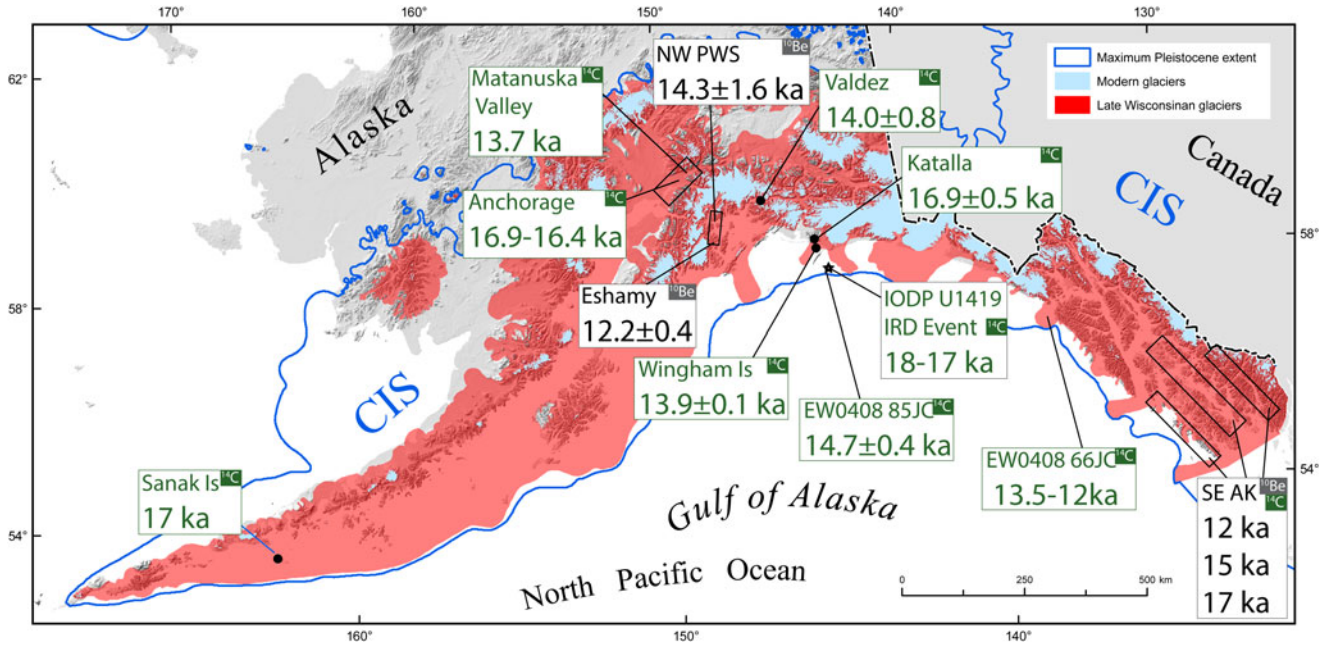

Figure 12. Map showing ages of late Quaternary deglaciation along the Alaskan margin. Boxes show deglaciation locality and ages. Ages in black are from cosmogenic surface exposure dates. Ages in green are earliest postglacial radiocarbon dates. Sources of data: Sanak Island from Misarti et al. (2012), Anchorage and Matanuska Valley from Kopczynski et al. (2017), Eshamy and NW Prince William Sound (PWS) from this study, Valdez from Reger (1990), Wingham Island from Chapman et al. (2009), Katalla from Sirkin and Tuthill (1987), southeastern Alaska (SE AK) from Lesnek et al. (2020), and IODP core U1419 from Walczak et al. (2020). Base map showing extent of late Wisconsinan (approximately last glacial maximum) and Pleistocene maximum extent of glaciers in Alaska, from Kaufman et al. (2011). Extent of Cordilleran Ice Sheet (CIS) in Canada from Batchelor et al. (2019).

excluding the Eshamy transect), and the ^{14}C age is slightly younger, as expected when allowing for the growth of vegetation. This older ^{14}C age is from a site near Valdez, 95 km away on the east side of PWS. The similarity of the ^{14}C and ^{10}Be ages suggests that the timing of deglaciation in eastern PWS is similar to western PWS, as one might expect because of the similar

https://doi.org/10.1017/qua.2021.33 Published online by Cambridge University Press

physiographic setting. The younger ^{14}C age (11,580 ± 220 cal yr BP; Heusser, 1983; Fig. 12, Table 1) is slightly younger than the average of our near sea-level samples (12.9 ± 1.1 ka; see also Fig. 8). The site for the younger ^{14}C age is about 10 km north of our northernmost samples (Fig. 2), which is consistent with the model of northward-retreating glaciers.

The timing of ice retreat of the CIS in PWS appears to be similar to some phases of ice retreat elsewhere along the southern Alaska margin. As mentioned earlier, Davies et al. (2011) interpreted core EW0408 85JC (Fig. 12) from offshore and southeast of PWS as having a transition from coarse glacial-marine sediments to finely laminated sediments at 14,790 ± 380 cal yr BP. They interpreted this date as the time that tidewater glaciers to the north retreated onto land or behind fjord sills. Their age is similar to our result. Due north of this core, at a terrestrial site in the coastal Katalla River valley (Figs. 2A and 12), Sirkin and Tuthill (1987) reported a postglacial radiocarbon age of 16,850 ± 550 cal yr BP (Table 1). This age implies deglaciation was locally underway along the coast east of PWS significantly earlier than in northern PWS or offshore. Chapman et al. (2009), in a study of Wingham Island, another coastal site 15 km east of Katalla and about 220 km to the east of our study sites (Figs. 1 and 12), obtained a ^{14}C age of 13,890 ± 80 cal yr BP (Table 1) on a terrace, close to modern sea level, which formed after ice retreat. The Wingham Island date is similar to the weighted mean of most of our ages of 14.3 ± 1.6 ka and is older than our sea-level site ages of 12.9 ± 1.1 ka. Given the proximity of the Wingham site to the Katalla River valley (25 km apart), the difference in the radiocarbon ages is surprising, with the Katalla River valley being deglaciated approximately 3000 yr earlier than the nearby and more distal Wingham Island site.

Sanak Island, which lies about 1100 km to the southwest of PWS (Fig. 12), provides another constraint for the timing of deglaciation on the southern Alaska margin. Misarti et al. (2012) studied lake cores and concluded that deglaciation initiated by ~17 ka, as indicated by radiocarbon and pollen data. Just north of PWS, on the leeward side of the Chugach Mountains in the Anchorage area, Kopczynski et al. (2017) found that initial retreat of glaciers (Figs. 1 and 12) occurred between 16.8 and 16.4 ka, and a second faster phase of retreat was completed by 13.7 ka. The older time period is very similar to the Sanak and Katalla ages, and the younger age is similar to both the Wingham Island age and our ages, which suggests that retreat of glaciers in the Anchorage area before 13.7 ka (Kopczynski et al., 2017) was almost synchronous with the main pulse of thinning in northern PWS. The Perry Island ages of 16.6 ± 2.3 and 17.4 ± 2.0 ka at our most oceanward site are similar to the older ages in the Anchorage area, suggesting that warming was concurrent on both sides of the Chugach Mountains, although the northern, drier side of the Chugach Mountains was deglaciated before the southern, wetter side of the mountains of northern PWS. This inference is consistent with the recent results of Valentino et al. (2021), who used cosmogenic isotopes to date deglaciation of higher-elevation sites (568–1678 m) within the Chugach Mountains near Anchorage and Valdez and obtained ages between ~26.7 ± 2.4 and 17.3 ±1.5 ka.

Southeastern Alaska ages of deglaciation show similar patterns. About 700 km southeast of PWS, Praetorius and Mix (2014) studied core EW0408 66JC offshore Cross Sound and inferred significant landward retreat of glaciers between ~13 and 12.5 ka based on changes in sediment type and radiocarbon dating (Fig. 12). This time period is similar to our sea-level ages. About 1000 km to the southeast of PWS, in the fjords of southern southeastern Alaska, Lesnek et al. (2020) found the most rapid phase of glacial retreat on the outer coast took place between ~17 and 15 ka, and most inner fjords were free of ice by 15 ka (Fig. 12). Their work utilized 40 ^{10}Be exposure ages and 25 radiocarbon ages and is currently the most robust terrestrial data set constraining deglaciation of the northern marine-terminating part of the CIS. The 17 ka age is the same as the Sanak Island age as well as the oldest phase of deglaciation in the Anchorage region. Despite the larger uncertainties in our data set, the younger southeast Alaska ^{10}Be ages appear to precede those of PWS by 1–2 ka. Because the oceanographic, storm trajectory, and bathymetric conditions of southeastern Alaska and PWS are similar, the higher latitude and higher mountains of northern PWS may be the cause of the difference in ages between the two regions.

The timing of ice retreat in PWS and other marine-terminating parts of the CIS was preceded by warming sea-surface temperatures. Praetorius et al. (2020) compiled records of northeastern Pacific sea-surface temperature data that show warming from 17 ka into the Bølling event, which started at 14.6 ka. The data show slight cooling through the Younger Dryas period, followed by warming at about 12.1 ka. These time periods and temperature transitions are reflected in the deglacial history in the North Pacific, with the oldest pulses of deglaciation around 17 ka in southern southeast Alaska, Katalla, the Anchorage region, and Sanak Island. Widespread, and perhaps catastrophic deglaciation occurred during the Bølling period in northern PWS, offshore in core EW0408 85JC, Wingham Island, Valdez, and slightly later in the Anchorage area (Fig. 12).

Our study contributes to a growing body of evidence that collapse of the CIS was an important precursor to global climate change events. As discussed earlier, the initial retreat of CIS marine-terminating glaciers was likely caused by ocean warming (Praetorius et al., 2015, 2020) and dramatic sea-level rise (Spratt and Lisiecki, 2016), with the later stages of deglaciation possibly driven by atmospheric warming (e.g., Shakun et al., 2012). Walczak et al. (2020) recently dated the presence of North Pacific ice-rafted debris (IRD) events at IODP Site U1419, about 200 km to the southeast of PWS (Fig. 12). The IRD events (termed "Siku events") are thought to indicate major ice sheet retreat. The events were constrained by 250 ^{14}C dates and are similar to the Heinrich events of the North Atlantic but predate them by 1370 ± 550 yr. The youngest of these IRD events was between 18,000 and 17,000 yr BP. This time is consistent with, and slightly older than, terrestrial postglacial ages from Sanak Island, the Anchorage area, the Katalla River valley, SE Alaska, and this study (Fig. 12). Thus, this study adds to the evidence that the collapse of the CIS was early in a sequence of global climate change events, postdating strong Asian monsoons and predating North Atlantic Heinrich events, Antarctic warming, and global CO_2 rise (Walczak et al., 2020).

Finally, our observations suggest a two-stage model for the development of the fjordland topography in PWS during glacial retreat. In the first stage at glacial maxima, ice flowed from the highest topography toward the middle of PWS, over lower topography, such as over the top of Perry Island (Fig. 5C). The bathymetry of the sound (Fig. 2) shows that ice flowed out via Hinchinbrook Entrance and Montague Strait, and it reached the edge of the continental shelf along cross-shelf troughs (e.g., Kaufman and Manley, 2004; Kaufmann et al., 2011). In the second stage, as marine-terminating trunk glaciers thinned and retreated, the glacial flow direction sometimes changed

https://doi.org/10.1017/qua.2021.33 Published online by Cambridge University Press

drastically. For example, the CFPW glacier (Fig. 2B) thinned, and ice flow oriented itself downhill of newly exposed mountainside slopes, perpendicular to the earlier flow direction (Fig. 4). The change in direction of ice flow from times of glacial maxima to a different direction after the retreat of tidewater glaciers explains the common large fjords and glacial valleys, which are cut at a high angle by younger and smaller glaciers in PWS topography.

The Quaternary history of this region is ripe for further study. With respect to improving the ^{10}Be record of deglaciation, a larger sample volume, boulder–bedrock pairs, and a denser sampling scheme would improve results and decrease errors. Granitic bedrock seems to be the most viable rock type for CRN dating, and additional granites in north-central and eastern PWS would make good targets. In addition, quantitative data are needed to constrain GIA (e.g., Shugar et al., 2014), and how GIA is modulated by a subduction megathrust directly below sites loaded with ice should be evaluated. Coring and high-precision ^{14}C dating in glacial troughs both offshore and within PWS are needed to gain data on the timing and conditions of deglaciation and to better evaluate the drivers of deglaciation.

CONCLUSIONS

This is the first ^{10}Be study of deglaciation in the PWS region of Alaska. We obtained 26 ^{10}Be surface-exposure ages from glacially scoured bedrock surfaces (Figs. 3 and 4). The samples were collected from six localities that span elevation transects where summits were rounded and overrun by LGM glaciers between sea level and 620 m. Ages range between 24.3 ± 2.5 and 8.8 ± 1.8 ka and average 14.0 ± 1.8 ka (Table 3). We evaluated the effects of snow cover on the ages and estimate shielding from snow cover would push the ages older by at least 400 yr. To assess the effects of GIA and sea-level rise and potential shielding on the exposure ages, we utilized the iceTEA set of tools (Jones et al., 2019a) and found these processes did not have a significant effect. Samples collected near sea level have ages consistent with being from a population that averages to 12.9 ± 1.1 ka.

We evaluated simple and more complex models of ice thinning and retreat. Of the six elevation transects, we found that only the Culross Island transect ages can be readily explained by a simple model of ice removal with oldest ages at the top and younger ages down low (Fig. 8). We evaluated deglaciation processes that would affect other age–elevation profiles (Fig. 9) and infer some sample ages were influenced by lingering snow and ice and possible cosmogenic inheritance. We were unable to directly test for ^{10}Be inheritance, because we were unable to find paired boulder and bedrock surfaces to sample. We culled additional ages that may have been affected by lingering ice and inheritance, and the remaining ages were between 17.4 ± 2.0 and 11.6 ± 2.8 ka.

We assessed rates of thinning and ice retreat from our sample transects. We calculated ice-thinning rates using a Monte Carlo approach implemented in the iceTEA calculator. We grouped data into four vertical transects and found thinning rates are between 120 and 160 m/ka based on the median and mode of the probability distributions (Fig. 10). We also found evidence of a correlation between the ages of each transect and the distance to the paleo–ice source. Considering all the sites and using the same Monte Carlo approach implemented in iceTEA, we calculated a retreat rate of 20 m/yr (Fig. 11). The Eshamy transect is unique among our sample transects, in that it is located closer to its paleo–ice source, the Sargent Icefield, than the other more northerly transects, which have an ice source in the College Fiord region. The Eshamy transect has a younger set of ages, which give a weighted mean of 12.2 ± 0.4 ka, in contrast to the mean of the ages from the other northerly sites of 14.3 ±1.6 ka. We infer this older age indicates when ice retreated from our sample sites in the mountains, and the sea-level weighted mean age of 12.9 ± 1.1 ka is the approximate time that tidewater glaciers retreated past the low-elevation sites in northern PWS. These ages are consistent with the two limiting radiocarbon ages for deglaciation in PWS. One of these ages is from the northeast side of the sound and, given its similarity to our ages, suggests that all parts of the sound had a similar deglaciation history.

Regional comparisons of these new ages show the timing of ice retreat in PWS appears to be similar to some phases of ice retreat elsewhere along the southern Alaska margin (Fig. 12). The thinning of the glaciers in northwestern PWS is within error of the time of retreat of glaciers on the northwest side of the Chugach Mountains in the Anchorage region, on Wingham Island to the southeast of PWS, and from cores offshore the Yakutat region and southeast Alaska. However, retreat of the marine-terminating glaciers, as indicated by the Eshamy transect, appears to be later, and may have been synchronous with collapse of part of the Sargant Icefield. Nonetheless, our study adds to a growing body of evidence that collapse of the CIS soon after 17 ka was early in a sequence of global climate change events, postdating strong Asian monsoons and predating North Atlantic Heinrich events, Antarctic warming, and global CO_2 rise (Walczak et al., 2020).

Acknowledgments. Thanks to Kara and Katie Haeussler for help in sample collection and to Keith Labay for help with drafting of some of the figures. Thanks to editor Derek Booth, associate editor Yeong Bae Seong, two anonymous reviewers, and John Jaeger for exceptionally constructive journal reviews; Adrian Bender, Sue Karl, Marti Miller, and Janet Slate for their reviews; and Jason Addison for additional input. Fieldwork was funded by the U.S. Geological Survey; the Hebrew University Jerusalem funded analysis of samples. Any use of trade, firm, or product names is for descriptive purposes only does not imply endorsement by the U.S. government.

REFERENCES

Arkle, J.C., Armstrong, P.A., Haeussler, P.J., Prior, M.G., Hartman, S., Sendziak, K.L., Brush, J.A., 2013. Focused exhumation in the syntaxis of the western Chugach Mountains and Prince William Sound, Alaska. *Geological Society of America Bulletin* **125**, 776–793.

Balbas, A.M., Barth, A.M., Clark, P.U., Clark, J., Caffee, M., O'Connor, J., Baker, V.R., Konrad, K., Bjornstad, B., 2017. ^{10}Be dating of late Pleistocene megafloods and Cordilleran ice sheet retreat in the northwestern United States. *Geology* **45**, 583–586.

Barclay, D.J., Wiles, G.C., Calkin, P.E., 2009. Holocene glacier fluctuations in Alaska. *Quaternary Science Reviews* **28**, 2034–2048.

Batchelor, C.L., Margold, M., Krapp, M., Murton, D.K., Dalton, A.S., Gibbard, P.L., Stokes, C.R., Murton, J.B., Manica, A., 2019. The configuration of Northern Hemisphere ice sheets through the Quaternary. *Nature Communications* **10**, 1–10.

Blanchet, D., 1983. *Chugach National Forest Environmental Atlas*. U.S. Forest Service Alaska Region Report 124.

Borchers, B., Marrero, S., Balco, G., Caffee, M., Goehring, B., Lifton, N., Nishiizumi, K., Phillips, F., Schaefer, J., Stone, J., 2016. Geological calibration of spallation production rates in the CRONUS-Earth project. *Quaternary Geochronology* **31**, 188–198.

Bradley, D.C., Kusky, T., Haeussler, P., Goldfarb, R., Miller, M.L., Dumoulin, J., Nelson, S.W., Karl, S., 2003. Geologic signature of early Tertiary ridge subduction in Alaska. In: Sisson, V.E., Roeske, S.M., Pavlis, T.L. (Eds.), *Geology of a Transpressional Orogen Developed during Ridge-Trench Interaction along the North Pacific Margin. Geological Society of America Special Paper* 371, 19–49.

https://doi.org/10.1017/qua.2021.33 Published online by Cambridge University Press

Briner, J.P., Swanson, T.W., 1998. Using inherited cosmogenic ^{36}Cl to constrain glacial erosion rates of the Cordilleran ice sheet. *Geology* **26**, 3–6.

Bronk Ramsey, C., 2017. OxCal Program. Version 4.3 [computer software]. Oxford Radiocarbon Accelerator Unit, University of Oxford, Oxford.

Brook, E.J., Kurz, M.D., Ackert, R.P., Jr., Denton, G.H., Brown, E.T., Raisbeck, G.M., Yiou, F., 1993. Chronology of Taylor Glacier advances in Arena Valley, Antarctica, using in situ cosmogenic ^{3}He and ^{10}Be. *Quaternary Research* **39**, 11–23.

Chapman, J.B., Haeussler, P.J., Pavlis, T.L., 2009. Quaternary uplift history of Wingham Island, south-central Alaska. In: Haeussler, P.J., Galloway, J.P. (Eds.), *Studies by the U.S. Geological Survey in Alaska, 2007*. U.S. Geological Survey Professional Paper 1760-B.

Clague, J.J., 2017. Deglaciation of the Cordillera of Western Canada at the end of the Pleistocene. *Cuadernos de Investigación Geográfica* **43**, 449–466.

Clague, J.J., James, T.S., 2002. History and isostatic effects of the last ice sheet in southern British Columbia. *Quaternary Science Reviews* **21**, 71–87.

Clark, P.U., Dyke, A.S., Shakun, J.D., Carlson, A.E., Clark, J., Wohlfarth, B., Mitrovica, J.X., Hostetler, S.W., McCabe, A.M., 2009. The Last Glacial Maximum. *Science* **325**, 10–713.

Corbett, L.B., Bierman, P.R., Rood, D.H., 2016. An approach for optimizing in situ cosmogenic ^{10}Be sample preparation. *Quaternary Geochronology* **33**, 24–34.

Corbett, L.B., Bierman, P.R., Wright, S.F., Shakun, J.D., Davis, P.T., Goehring, B.M., Halsted, C.T., Koester, A.J., Caffee, M.W., Zimmerman, S.R., 2019. Analysis of multiple cosmogenic nuclides constrains Laurentide Ice Sheet history and process on Mt. Mansfield, Vermont's highest peak. *Quaternary Science Reviews* **205**, 234–246.

Darvill, C.M., Menounos, B., Goehring, B.M., Lian, O.B., Caffee, M.W., 2018. Retreat of the western Cordilleran ice sheet margin during the last deglaciation. *Geophysical Research Letters* **45**, 9710–9720.

Davies, M.H., Mix, A.C., Stoner, J.S., Addison, J.A., Jaeger, J., Finney, B. and Wiest, J., 2011. The deglacial transition on the southeastern Alaska Margin: Meltwater input, sea level rise, marine productivity, and sedimentary anoxia. *Paleoceanography*, **26**, doi:10.1029/2010PA002051.

Dyke, A.S., Moore, A., Robertson, L., 2003. Deglaciation of North America: Thirty Two Digital Maps at 1:7,000,000 Scale with Accompanying Digital Chronological Database and One Poster (Two Sheets) with Full Map Series. Geological Survey of Canada Open File 1574.

Erlandson, J.M., Torben, C.R., Braje, T.J., Casperson, M., Culleton, B., Fulfrost, B., Garcia, T., *et al.*, 2011. Paleoindian seafaring, maritime technologies, and coastal foraging on California's Channel Islands. *Science* **331**, 1181–1185.

Ferguson, K.M., Armstrong, P.A., Arkle, J.C., Haeussler, P.J., 2015. Focused rock uplift above the subduction décollement at Montague and Hinchinbrook Islands, Prince William Sound, Alaska. *Geosphere* **11**, 144–159.

Gilbert, G.K., 1904. Domes and dome structure of the High Sierra. *Bulletin of the Geological Society of America* **15**, 29–36.

Haeussler, P.J., Armstrong, P.A., Liberty, L.M., Ferguson, K.M., Finn, S.P., Arkle, J.C., Pratt, T.L., 2015. Focused exhumation along megathrust splay faults in Prince William Sound, Alaska. *Quaternary Science Reviews* **113**, 8–22.

Heusser, C.J., 1983. Holocene vegetation history of the Prince William Sound region, south-central Alaska. *Quaternary Research* **19**, 337–355.

Ivy-Ochs, S., Briner, J.P., 2014. Dating disappearing ice with cosmogenic nuclides. *Elements* **10**, 351–356.

Johnson, J.S., Bentley, M.J., Smith, J.A., Finkel, R., Rood, D., Gohl, K., Balco, G., Larter, R.D., Schaefer, J., 2014. Rapid thinning of Pine Island Glacier in the early Holocene. *Science* **343**, 999–1001.

Jones, R.S., Small, D., Cahill, N., Bentley, M.J., Whitehouse, P.L., 2019a. iceTEA: tools for plotting and analyzing cosmogenic-nuclide surface-exposure data from former ice margins. *Quaternary Geochronology* **51**, 72–86.

Jones, R.S., Whitehouse, P.L., Bentley, M.J., Small, D., Dalton, A.S., 2019b. Impact of glacial isostatic adjustment on cosmogenic surface-exposure dating. *Quaternary Science Reviews* **212**, 206–212.

Kaufman, D.S., Manley, W.F., 2004. Pleistocene maximum and Late Wisconsinan glacier extents across Alaska, USA. In: Ehlers, J., Gibbard, P.L. (Eds.), *Developments in Quaternary Sciences*. Vol. 2, Part B. Elsevier, London, pp. 9–27.

Kaufman, D.S., Young, N.E., Briner, J.P., Manley, W.F., 2011. Alaska palaeo-glacier atlas (version 2). In: Ehlers, J., Gibbard, P.L., Hughes, P.D. (Eds.), *Developments in Quaternary Sciences*. Vol. 15. Elsevier, London, pp. 427–445.

Kohl, C.P., Nishiizumi, K., 1992. Chemical isolation of quartz for measurement of in-situ-produced cosmogenic nuclides. *Geochimica et Cosmochimica Acta* **56**, 3583–3587.

Kopczynski, S.E., Kelley, S.E., Lowell, T.V., Evenson, E.B., Applegate, P.J., 2017. Latest Pleistocene advance and collapse of the Matanuska–Knik glacier system, Anchorage Lowland, southern Alaska. *Quaternary Science Reviews* **156**, 121–134.

Larsen, C.F., Motyka, R.J., Freymueller, J.T., Echelmeyer, K.A., Ivins, E.R., 2005. Rapid viscoelastic uplift in southeast Alaska caused by post-Little Ice Age glacial retreat. *Earth and Planetary Science Letters* **23**, 548–560.

Lesnek, A.J., Briner, J.P., Baichtal, J.F., Lyles, A.S., 2020. New constraints on the last deglaciation of the Cordilleran Ice Sheet in coastal Southeast Alaska. *Quaternary Research* **96**, 140–160.

Lifton, N., Sato, T., Dunai, T.J., 2014. Scaling in situ cosmogenic nuclide production rates using analytical approximations to atmospheric cosmic-ray fluxes. *Earth and Planetary Science Letters* **386**, 149–160.

Lowell, T.V., 1995. The application of radiocarbon age estimates to the dating of glacial sequences: an example from the Miami sublobe, Ohio, USA. *Quaternary Science Reviews* **14**, 85–99.

Mackintosh, A., White, D., Fink, D., Gore, D.B., Pickard, J., Fanning, P.C., 2007. Exposure ages from mountain dipsticks in Mac. Robertson Land, East Antarctica, indicate little change in ice-sheet thickness since the Last Glacial Maximum. *Geology* **35**, 551–554.

Mandryk, C.A.S., Josenhans, H., Fedje, D.W., Mathewes, R.W., 2001. Late Quaternary paleoenvironments of northwestern North America: implications for inland versus coastal migration routes. *Quaternary Science Reviews* **20**, 301–314.

Marrero, S.M., Phillips, F.M., Borchers, B., Lifton, N., Aumer, R., Balco, G., 2016. Cosmogenic nuclide systematics and the CRONUScalc program. *Quaternary Geochronology* **31**, 160–187.

Menounos, B., Goehring, B.M., Osborn, G., Margold, M., Ward, B., Bond, J., Clarke, G.K., *et al.*, 2017. Cordilleran Ice Sheet mass loss preceded climate reversals near the Pleistocene Termination. *Science* **358**, 781–784.

Misarti, N., Finney, B.P., Jordan, J.W., Maschner, H.D.G., Addison, J.A., Shapely, M.D., Krumhardt, A., Beget, J., 2012. Early retreat of the Alaska Peninsula Glacier Complex and the implications for coastal migrations of First Americans. *Quaternary Science Reviews* **48**, 1–6.

Nelson, S.W., Dumoulin, J.A., Miller, M.L., 1985. Geologic map of the Chugach National Forest, Alaska. U.S. Geological Survey Miscellaneous Field Studies Map MF-1645-B. 1:250,000. U.S. Geological Survey, Reston, VA.

Peltier, W.R., Argus, D.F., Drummond, R., 2015. Space geodesy constrains ice age terminal deglaciation: the global ICE-6G_C (VM5a) model. *Journal of Geophysical Research: Solid Earth* **120**, 450–487.

Plafker, G., 1969. *Tectonics of the March 27, 1964, Alaska Earthquake*. U.S. Geological Survey Professional Paper 543-I, pp. 1–74.

Plafker, G., Moore, J.C., Winkler, G., 1994. Geology of the southern Alaska margin. In: Plafker, G., Berg, H.C. (Eds.), *The Geology of Alaska*. Vol. G-1, *Geology of North America*. Geological Society of America, Boulder, CO, pp. 389–449.

Praetorius, S.K., Condron, A., Mix, A.C., Walczak, M.H., McKay, J.L. Du, J., 2020. The role of Northeast Pacific meltwater events in deglacial climate change. *Science Advances* **6**, eaay2915.

Praetorius, S.K., Mix, A.C., 2014. Synchronization of North Pacific and Greenland climates preceded abrupt deglacial warming. *Science* **345**, 444–448.

Praetorius, S.K., Mix, A.C., Walczak, M.H., Wolhowe, M.D., Addison, J.A., Prahl, F.G., 2015. North Pacific deglacial hypoxic events linked to abrupt ocean warming. *Nature* **527**, 362–366.

Reger, R.D., 1990, *Deglaciation of the Allison-Sawmill Creeks Area, Southern Shore of Port Valdez, Alaska*. Alaska Division of Geological and Geophysical Surveys Professional Report 111, pp. 55–59.

Reimer, P.J., Bard, E., Bayliss, A., Beck, J.W., Blackwell, P.G., Ramsey, C.B., Buck, C.E., *et al.*, 2013. IntCal13 and Marine13 radiocarbon age calibration curves 0–50,000 years cal BP. *Radiocarbon* **55**, 1869–1887.

Seguinot, J., Khroulev, C., Rogozhina, I., Stroeven, A.P., Zhang, Q., 2014. The effect of climate forcing on numerical simulations of the Cordilleran Ice Sheet at the Last Glacial Maximum. *Cryosphere* **8**, 1087–1103.

https://doi.org/10.1017/qua.2021.33 Published online by Cambridge University Press

Seguinot, J., Rogozhina, I., Stroeven, A.P., Margold, M., Kleman, J., 2016. Numerical simulations of the Cordilleran Ice Sheet through the last glacial cycle. *Cryosphere,* **10**, 639–664.

Shakun, J.D., Clark, P.U., He, F., Marcott, S.A., Mix, A.C., Liu, Z., Otto-Bliesner, B., Schmittner, A., Bard, E., 2012. Global warming preceded by increasing carbon dioxide concentrations during the last deglaciation. *Nature* **484**, 49.

Shennan, I., Bruhn, R., Barlow, N., Good, K., Hocking, E., 2014. Late Holocene great earthquakes in the eastern part of the Aleutian megathrust. *Quaternary Science Reviews* **84**, 86–97.

Shugar, D.H., Walker, I.J., Lian, O.B., Eamer, J.B., Neudorf, C., McLaren, D., Fedje, D., 2014. Post-glacial sea-level change along the Pacific coast of North America. *Quaternary Science Reviews* **97**, 170–192.

Shulski, M., Wendler, G., 2007. *The Climate of Alaska*. University of Alaska Press, Fairbanks.

Sirkin, L., Tuthill, S.J., 1987. Late Pleistocene and Holocene deglaciation and environments of the southern Chugach Mountains, Alaska. *Geological Society of America Bulletin* **99**, 376–384.

Spratt, R.M., Lisiecki, L.E., 2016. A late Pleistocene sea level stack. *Climate of the Past* **12**, 1079–1092.

Stone, J.O., Balco, G.A., Sugden, D.E., Caffee, M.W., Sass, L.C., Cowdery, S.G., Siddoway, C., 2003. Holocene deglaciation of Marie Byrd Land, West Antarctica. *Science* **299**, 99–102.

Stroeven, A.P., Fabel, D., Margold, M., Clague, J.J., Xu, S., 2014. Investigating absolute chronologies of glacial advances in the NW sector of the Cordilleran Ice Sheet with terrestrial in situ cosmogenic nuclides. *Quaternary Science Reviews* **92**, 429–443.

Valentino, J.D., Owen, L.A., Spotila, J.A., Cesta, J.M., Caffee, M.W., 2021. Timing and extent of Late Pleistocene glaciation in the Chugach Mountains, Alaska. *Quaternary Research* **101**, 205–224.

Vieli, A., Nick, F.M., 2011. Understanding and modelling rapid dynamic changes of tidewater outlet glaciers: issues and implications. *Surveys in Geophysics* **32**, 437–458.

Walczak, M.H., Mix, A.C., Cowan, E.A., Fallon, S., Fifield, L.K., Alder, J.R., Du, J., *et al.*, 2020. Phasing of millennial-scale climate variability in the Pacific and Atlantic Oceans. *Science* **370**, 716–720.

Wiles, G.C., Barclay, D.J., Calkin, P.E., 1999. Tree-ring-dated "Little Ice Age" histories of maritime glaciers from western Prince William Sound, Alaska. *The Holocene* **9**, 163–173.

Young, N.E., Lamp, J., Koffman, T., Briner, J.P., Schaefer, J., Gjermundsen, E.F., Linge, H., *et al.*, 2018. Deglaciation of coastal southwestern Spitsbergen dated with in situ cosmogenic ^{10}Be and ^{14}C measurements. *Journal of Quaternary Science* **33**, 763–776.

Zimmermann, M., Prescott, M.M., Haeussler, P.J., 2019. Bathymetry and geomorphology of Shelikof Strait and the western Gulf of Alaska. *Geosciences* **9**, 409.

https://doi.org/10.1017/qua.2021.33 Published online by Cambridge University Press